Low Voltage Ride Through Enhancement of Doubly Fed Induction Generator Wind Turbines with Fuzzy Logic Controlled Crowbar and Series Dynamic Braking Resistor

Asmelash Mebrahtu Tesfay

A Thesis Submitted to the department of Electrical Power and Control Engineering

School of Electrical Engineering and Computing

Presented in Partial Fulfilment of the Requirement for the Degree of Master's in Electrical Power and Control Engineering (Power System Engineering)

Office of Graduate Studies

Adama Science and Technology University

September, 2024

Adama, Ethiopia

Low Voltage Ride Through Enhancement of Doubly Fed Induction Generator Wind Turbines with Fuzzy Logic Controlled Crowbar and Series Dynamic Braking Resistor

Asmelash Mebrahtu Tesfay

Advisor: Dr. Tafesse Asrat

A Thesis Submitted to the department of Electrical Power and Control Engineering

School of Electrical Engineering and Computing

Presented in Partial Fulfilment of the Requirement for the Degree of Master's in Electrical Power and Control Engineering (Power System Engineering)

Office of Graduate Studies

Adama Science and Technology University

September, 2024

Adama, Ethiopia

DECLARATION

I hereby declare that this Master Thesis entitled "Low Voltage Ride Through Enhancement of Doubly Fed Induction Generator Wind Turbines with Fuzzy Logic Controlled Crowbar and Series Dynamic Braking Resistor" is my original work. That is, it has not been submitted for the award of any academic degree, diploma or certificate in any other university. All sources of materials that are used for this thesis have been duly acknowledged through citation.

Asmelash Mebrahtu Tesfay	____________________	____________________
Name of student	Signature	Date

RECOMMENDATION

I, the advisor of this thesis, hereby certify that I have read the revised version of the thesis entitled “Low Voltage Ride Through Enhancement of Doubly Fed Induction Generator Wind Turbines with Fuzzy Logic Controlled Crowbar and Series Dynamic Braking Resistor” prepared under my guidance by Asmelash Mebrahtu Tesfay submitted in partial fulfilment of the requirements for the degree of Master’s of Science in Electrical Power and Control Engineering (Power System Engineering). Therefore, I recommend the submission of a revised version of the thesis to the department following the applicable procedures.

____________________	____________________	____________________
Advisor	Signature	Date

APPROVAL PAGE

I, the advisor of the thesis entitled "Low Voltage Ride Through Enhancement of Doubly Fed Induction Generator Wind Turbines with Fuzzy Logic Controlled Crowbar and Series Dynamic Braking Resistor" developed by Asmelash Mebrahtu Tesfay, hereby certify that the recommendation and suggestions made by the board of examiners are appropriately incorporated into the final version of the thesis.

Advisor	Signature	Date

We, the undersigned, members of the Board of Examiners of the thesis by Asmelash Mebrahtu Tesfay have read and evaluated the thesis entitled "Low Voltage Ride Through Enhancement of Doubly Fed Induction Generator Wind Turbines with Fuzzy Logic Controlled Crowbar and Series Dynamic Braking Resistor" and examined the candidate during open defense. This is, therefore, to certify that the thesis is accepted for partial fulfilment of the requirement of the degree of Master of Science in Electrical Power and Control Engineering (Power System Engineering).

Chairperson	Signature	Date
Dr. Negasa Muleta		09/24/2024
Internal Examiner	Signature	Date
Dr. Wondwossen Astatike		09/23/2024
External Examiner	Signature	Date

Final approval and acceptance of the thesis is contingent upon submission of its final copy to the Office of Postgraduate Studies (OPGS) through the Department Graduate Council (DGC) and School Graduate Committee (SGC).

Department Head	Signature	Date
School Dean	Signature	Date
Office of Postgraduate Studies, Dean	Signature	Date

ACKNOWLEDGEMENTS

I need to express my special thanks to my advisor, Dr. Tafesse Asrat for his persistent advice and encouragement during this thesis work. I am also pleased to thank my maintenance and operation team co-workers from the Adama II wind power plant for their invaluable assistance and support in this study. Moreover, I would also like to thank my parents and friends for their endless support and inspiration during this research period.

TABLE OF CONTENTS

LIST OF TABLES

LIST OF FIGURES

LIST OF ABBREVIATIONS

AC	Alternating Current
BESS	Battery Energy Storage System
DC	Direct Current
DFIG	Doubly Fed Induction Generator
DPC	Direct Power Control
DTC	Direct Torque Control
DVR	Dynamic Voltage Restorer
FACTS	Flexible AC Transmission System
FLC	Fuzzy Logic Controller
FRT	Fault Ride Through
GSC	Grid Side Converter
IGBT	Insulated Gate Bipolar Transistor
IVC	Indirect Vector Control
LCL	Inductive Capacitive Inductive Filter
LVRT	Low Voltage Ride Through
MPPT	Maximum Point Power Tracking
MSC	Machine Side Converter
PCC	Point of Common Coupling
PEC	Power Electronic Converter
POI	Point of Interconnection
RSC	Rotor Side Converter
SCIG	Squirrel Cage Induction Generator
SDBR	Series Dynamic Braking Resistor

STATCOM	Static Synchronous Compensator
TSO	Transmission System Operators
WECS	Wind Energy Conversion System
WRIG	Wound Rotor Induction Generator
WTGS	Wind Turbine Generator System

ABSTRACT

Doubly fed induction generator (DFIG) type wind turbines are widely used nowadays as they offer benefits such as low-cost power electro-converters, different speed operations, separate control of reactive and active powers, and reduced filter requirements. However, the direct coupling of their stator winding to the power network and utilisation of small back-to-back converter power ratings make them highly susceptible to power network faults, particularly voltage drops. When these generators sense voltage dips at the point of interconnection (POI), their stator voltage diminishes immediately, which further causes oscillation of the stator as well as rotor currents, DC bus over-voltage, and torque fluctuations. This may produce damage to the generator stator and rotor circuits, including the fault-prone converters. In the past years, these wind turbine-type generators were rapidly isolated in the event of severe voltage sags. As their installation is significantly increasing, transmission system operators (TSO) need them to stay coupled with the grid and provide support in maintaining voltage stability, currently. The ability of wind turbine generators to keep connected to power system networks under severe voltage sags is named to as low voltage ride-through capability. To fulfil such capacity while withstanding the aforementioned challenges, an appropriate enhancing scheme or protection should be applied. Hence, in this thesis, a hybrid fuzzy logic controlled (FLC) crowbar and series dynamic braking resistor is employed. The DFIGs' performance under steady as well as transient states with this improving technique was examined. To observe its effectiveness, this scheme was compared with the conventional and fuzzy logic-controlled (FLC) crowbars under 90% symmetrical voltage dips for 150 milliseconds. The torque control loss was preserved at 3 seconds, 3.44 seconds, and 4.1 seconds with FLC combined crowbar and SDBR, FLC crowbar, and conventional crowbar following the dip at 2.5 seconds, respectively. The stator voltage was stabilised at 4 seconds, 3.48 seconds, and 3.2 seconds using the traditional crowbar, FLC crowbar and FLC hybrid crowbar and SDBR correspondingly. The rotor current, however, regains its nominal value at 3 seconds, 3.44 seconds, and 4.1 seconds employing the hybrid FLC crowbar and SDBR, FLC crowbar, and conventional crowbar, respectively. As a result, the hybrid FLC crowbar and SDBR perform better LVRT capability-enhancing schemes. The primary data were taken from Adama II wind power, and MATLAB/Simulink 2021a software was used for modelling and simulation.

Keywords: Series Dynamic Braking Resistor, Fuzzy Logic Control, Crowbar, DFIG, Low Voltage Ride Through, MATLAB/Simulink

CHAPTER 1

INTRODUCTION

1.1. Background

Due to the rising need for electricity and climate change concerns, the search for sustainable and clean sources of energy such as wind, solar, hydro, and geothermal is becoming an important topic for the International Energy Agency (IEA) in many countries (Padhi et al., 2019). Frequent use of traditional energy sources such as fossil fuel leads to a rise in the environmental temperature globally, however, utilizing these renewable energy sources mitigates this atmospheric issue. Wind energy is among the most available, exploitable, and rapid-developing green technologies. As a result, it is targeted as one of the largest energy contributions to future power supply (Khan et al., 2021).

A wind power produces energy by extricating the kinetic energy in the wind through its rotor blades into mechanical ones and then converting it to electrical using electrical generators. Considering the generator type used, the applied power electronics, and their rotor speed operations, wind turbines can be classified into fixed speed (Type-1 WTGS), partial variable (Type-2 WTGS), and variable (Type-3 and 4 WTGS) turbines (Wu & Sun, 2018; Xu et al., 2018). In variable-speed rotor operations, maximum energy conversion is attained efficiently from a large extent of wind speeds. Thus, Type-3 WTGS (Doubly Fed Induction Generator) and Type 4-WTGS (Permanent Magnet Synchronous Generator) are the two promising wind power in the wind turbine industry. A DFIG is an asynchronous generator with a wound rotor and slip-rings that supply electrical power with its stator and rotor terminals.

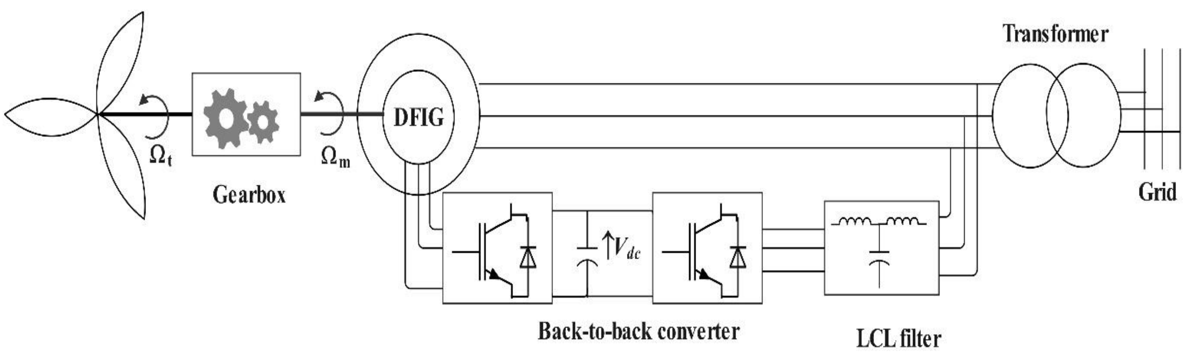

Figure 1.1: DFIG Based Wind Power Generator System (WPGS) (ABB, 2017)

As delineated in Figure 1.1, the DFIG stator is linked to the power network directly while its rotor is coupled using a back-to-back converter.

The DFIG possesses lower converter loss and cost, can run at various speeds, requires reduced filter size, injects low harmonics to the power network, and controls its active as well as reactive powers independently. As a result, this generator is mostly preferred over type 4-WTGS types (Din et al., 2021).

Even though this wind turbine has the above-mentioned merits, it is highly susceptible to power grid faults, especially to voltage drops as its stator windings are directly connected to the power network. When voltage dips happen at the point of interconnection (POI), the DFIG become demagnetized/its stator flux will be reduced with the voltage drop. This flux reduction results in inrushing both its stator as well as rotor currents. Consequently, it will result damage to the stator and rotor circuits including the generator itself, its back-to-back power converters, and the whole system as well (Jayanthi & Devaraj, 2019). In such happenings, the converters must be disconnected as their ratings are typically smaller than the rotor fault currents which will lead the wind turbine to cut off from the grid.

However, many countries are employing a grid code requirement to maintain the WTGS united with the power system network during voltage sags. The capability of electric generators to stay connected in short periods of voltage dips is known as low voltage ride-through (LVRT) (Djidel et al., 2022). So, this project is intended to enhance the LVRT capability of the DFIG wind power in Adama II as they are facing the previously illustrated problems continuously.

1.2. Statement of the Problem

Owing to the straightforward coupling of their stator terminals to the power network and limited capacity of back-to-back power electronic converters, DFIG wind power plants are more sensitive to power network faults. During a short circuit happening on the power network, a voltage dip at the POI occurs and results in the loss of the internal magnetization of the generator relative to the lost voltage immediately. This demagnetisation leads to inrushing current at both the stator as well as rotor circuits, and DC bus over voltages. Adama II wind power plant has 102 DFIG-type wind turbine generators. In the last four years, as referred in Appendix E, 51 of these generators have faced broken of their rotor terminals and/or burn out of their slip rings and 93 of them short circuit on their back-to-back converter IGBT modules and/or DC bus fuse failures due to DC bus overvoltage as well as rotor overcurrent caused by voltage dips. 58 of these wind turbines had also experienced defects on their crowbar IGBT module because of the previously stated issue.

Moreover, four wind turbine generators had faced open/short circuits at their stator terminals as a result of stator overcurrent. So, this project has applied an effective measure of protection and control approach to mitigate the above-stated problems while satisfying the LVRT specifications during voltage sags.

1.3. Objective

1.3.1. General Objective

The goal of this thesis work is to enhance the LVRT capability of DFIG-based wind powers under transient conditions.

1.3.2. Specific Objectives

The explicit aims of this project are to:

- ✓ Examine the behaviour of DFIG-based wind turbines during steady as well as transient periods.
- ✓ Improve the transient stability of these wind turbines under voltage drops.
- ✓ Compare the FLC hybrid LVRT enhancing scheme with a FLC crowbar and the traditional crowbar one.
- ✓ Conclude and recommend according to the compared analysis.

1.4. Significance of the Study

This project is relevant to enhance the faults such as high stator as well rotor currents, and DC link overvoltage caused by grid voltage drops with the implementation of a hybrid FLC crowbar and series dynamic braking resistor to satisfy the grid code requirements of DFIG wind turbines. So, this thesis work directly benefits DFIG wind turbine owners including Ethiopian Electric Power.

1.5. Scope of the Study

This project targets on evaluating the performance of DFIG and enhancing its LVRT capability with appropriately controlled protection schemes during symmetrical voltage drops at the power network terminal.

The WTGS parameters including the generator, its power electronic back-to-back converter, DC link, and so on were taken from the Adama II wind power plant, and the entire system was simulated in MATLAB/Simulink software.

1.6. Thesis Outline

This thesis includes five sections. The current chapter gives information on the introduction to DFIG WTGS, the problem statement, the project objectives, significance of the study, and the thesis scope. Wind turbine technology types, grid code requirements, the performance of DFIG under symmetrical voltage sags, and various related LVRT enhancing techniques are reviewed in chapter two. Chapter three is all about the mathematical modelling of DFIG wind turbine system including the generator itself, its back-to-back converters and their control methods. The SDBR is also modelled in this chapter. The DFIG behaviour during steady state and symmetrical voltage sags are simulated and analysed in chapter four. The behaviour of DFIG implementing the traditional crowbar, FLC crowbar, and hybrid FLC crowbar with SDBR are also compared under the grid voltage drops. The last section provides a conclusion based on the comparative analysis of the above-listed enhancing techniques.

CHAPTER 2

LITERATURE REVIEW

In this chapter different surveys on DFIG wind turbine and its LVRT capability-enhancing techniques were reviewed.

2.1. Literature Search

Doubly-fed induction generator (DFIG) wind turbines are becoming dominant in the wind power industry as they offer low converter costs and wide speed operation ranges (Zou et al., 2019). These generators supply electric power to the grid directly through their stator and use a back-to-back converter with their rotor terminals.

However, the direct coupling of their stator terminal to the power network and the restricted capacity of their back-to-back converter make them vulnerable to grid faults like voltage drops. During voltage sags, the generator stator voltage drops immediately and results in stator flux reduction. This incident provokes to elevate of both the stator and rotor current flows since they are electromagnetically coupled. Thus, the inrushing stator overcurrent may result in damage to the stator conductors, while the overshoot in rotor current leads to an increase in the DC link voltage which further causes defects on the back-to-back partial converters (Davoudi et al., 2019). In the past, when the grid-connected DFIGs were relatively small compared to nowadays, wind turbine operators used to disconnect these wind power generators to protect them from grid faults. As the current power grids employ more DFIG wind turbines, stopping these generators during network faults would deepen the voltage dips so that they are no longer permissible according to the updated grid codes requirement (El Archi et al., 2019; Fdaili et al., 2020). As a result, keeping WTGS coupled to the grid and providing support in transitory periods which is all about LVRT capability in wind powers is now compulsory. According to different literature, the LVRT-improving methods of DFIG wind power plants are categorised as external hardware and internal control (software) based solutions (Sarwar et al., 2019). These hardware-based solutions can also be divided into external stator as well as rotor side approaches. The stator side contains SDBR, and reactive power compensation with Flexible AC Transmission devices (DVR, static var compensator (SVC), STATCOM, and so on).

On the other hand, the rotor side approach such as DC chopper, crowbar, Battery Energy Storage System (BESS), and Series Dynamic Resistor (SDR).

However, using these FACTs as an enhancing method raises the complexity and costs of the system (Jayanthi & Devaraj, 2019). The internal control enhancing techniques furtherly may also be classified as wind turbine control methods like Blade Pitch Angle (BPA), and back-to-back DFIG converter control techniques such as Sliding Mode Control (SMC), IVC, DTC, and DPC. These software-based improvement approaches are incapable of enhancing dips beyond mild voltage drops (WANG et al., 2018; Zou et al., 2019).

(Rauth et al., 2020) had carried out comparative analysis on crowbar, stator /rotor connected SDBR, DC chopper, BESS and DVR as LVRT capability enhancing techniques of DFIG. The stator overcurrent was better limited by applying DVR and stator connected SDBR while the rotor inrush current was damped well using crowbar and DVR. DC chopper and BESS stabilise the DC link voltage significantly, however, they did not decrease the rotor as well as stator overcurrent at all. Overall, the DVR approach has exhibited better performance compared to other schemes. However, its implementation requires a high initial cost.

(Ganthia et al., 2020) examined the LVRT enhancing capability of DFIG with shunt-connected FACT devices. Using the overall performance, controller complexity and cost as a specified comparison requirement, a STATCOM was preferred as effective and most reliable LVRT improving technique. But, this device demands a high initial cost.

(Jayanthi & Devaraj, 2019) performed a study on the performance of DFIG-based wind turbines by comparing with and without crowbar protections under grid voltage drops. The result was verified with MATLAB/Simulink software and the high fault current was damped by applying the crowbar protection. Nevertheless, using a crowbar as an improving technique prolongs the stator voltage recovery as its activation results in the absorption of reactive power from the grid.

(Rini Ann Jerin et al., 2018) had reviewed various hardware as well as internal traditional/advanced control LVRT improving approaches and made a comprehensive comparison based on their complexity, cost, and fault ride through enhancing capability. After all, they concluded that irrespective of the converter loss, crowbar-based protection gives a successful FRT solution. At the same time, their work ended by recommending hybrid crowbar-based improvement approaches for future researchers.

In (Okedu et al., 2011) SDBR was applied in series with the DFIG stator terminal to enhance the generator fault ride-through (FRT) capability.

The simulation analysis was done using PSCAD/EMTDC and the terminal voltage was effectively improved. Nonetheless, the DC bus voltage was not damped as required.

(Endale & Tuka, 2021) minimised the magnitudes of fault rotor current and DC overvoltage employing a combination of crowbar and BESS as an LVRT-improving scheme. The whole system was modelled and analysed with a MATLAB/Simulink environment.

However, the magnitudes of inrush stator current were high enough and voltages were not improved as demanded even with the listed hybrid enhancing scheme.

(Jayasawal & Thapa, 2021) enhanced the LVRT capability of DFIG wind turbines by regulating the fault rotor current and DC bus overvoltage using a hybrid crowbar and chopper. Even though the rotor side circuit parameters were stabilised following voltage dips, the stator parameters such as stator voltage, current and flux were not investigated.

So, the gaps in the above-written reviewed literature are summarised in Table 2.1 below.

Table 2.1: Summary of Surveyed Literature

<table>
<tr><th>Authors</th><th>LVRT improving schemes</th><th>Strength</th><th>Weakness</th></tr>
<tr><td>(Rauth et al., 2020)</td><td>DVR</td><td>DC bus voltage, stator, as well as rotor currents were stabilised</td><td rowspan="2">High initial cost</td></tr>
<tr><td>(Ganthia et al., 2020)</td><td>STATCOM</td><td>Stator voltage was enhanced well.</td></tr>
<tr><td>(Jayanthi & Devaraj, 2019)</td><td>Crowbar</td><td>The DC link voltage as well as rotor current were maintained.</td><td>Prolongs the grid voltage recovery, transient stator and rotor currents.</td></tr>
<tr><td>(Okedu et al., 2011)</td><td>SDBR</td><td>Damps the fault stator current as required.</td><td>Unable to stabilise the DC bus voltage.</td></tr>
<tr><td>(Endale & Tuka, 2021)</td><td>Crowbar and BESS</td><td rowspan="2">The DC link voltage as well as rotor current were maintained.</td><td rowspan="2">The magnitude of fault stator current is extremely high</td></tr>
<tr><td>(Jayasawal & Thapa, 2021)</td><td>Crowbar and chopper</td></tr>
</table>

Thus, in this project, considering the aforementioned literature gaps and the stated problem in chapter one, a hybrid fuzzy logic-controlled crowbar and SDBR protection are devoted to enhance the LVRT capability of DFIG-type wind turbines.

2.2. Wind Turbine Generation System

A wind turbine generation system (WTGS) is an arrangement that converts the kinetic energy of the wind into mechanical one with its turbine rotor and then this mechanical energy is further altered to electrical energy with the help of a generator (Amirul Bin Mohd Adnan et al., 2022).

2.2.1. Elements of Wind Turbines

A wind power contains a tower, nacelle, rotor, gearbox, transmission, power electronic interface, control system, anemometer, wind vane, and unit transformer.

A tower is used to install the turbine's generator at a longer height to capture more energy through getting higher wind speeds.

The generator, yawing operation and hydraulic systems are housed in the nacelle. The energy from the wind is extracted and converted to mechanical one by the rotor.

The transmission increases the high torque slow speed of the rotor to the high rotation speed shaft of the generator. The mechanical energy produced by the rotor is converted to electrical one by a generator and typically has a stator as well as a rotor winding. The rotor is in charge of the created magnetic field and is the rotating part while the stator is responsible for mounting the coil wires and is stationary. It could be either a synchronous or asynchronous (induction) generator.

The generated power is supplied into the power network through its rotor via a power electronic converter. On the machine side, this converter assures that the turbine running speed is repeatedly adjusted to extract optimum power out of the wind following a maximal tracking point. On the network side, the PEC should fulfil the grid code requirements irrespective of the wind speed, such as the ability to control voltage, frequency, and active as well as reactive power. A wind turbine system control ensures proper working of the WTGS under all operational conditions. The anemometer instruments the wind speed, while the wind direction is scoped by the wind vane. The unit transformer steps up and down the voltage magnitude during generator excitation and power extraction to the grid respectively (Al-Majed & Fujigaki, 2010).

2.3. Wind Turbine Generator System (WTGS) Technology

Wind turbine designs have developed from fixed speed, passively controlled and drive trains with gearboxes, to become variable speed, active-controlled with or without gearboxes, using the latest in power electronics, aerodynamics, and mechanical drive train designs (Hiremath & Moger, 2020).

According to their speed controllability, generator type, and power electronics wind turbines may be classified into the following four main types.

2.3.1. Fixed Speed WTGS

This is the oldest, simplest, and most robust design. However, it works at a fixed speed since its hilly speed- torque peculiar of the induction generator and the energy capture from the wind cannot be optimized.

As displayed in Figure 2.1, it incorporates a power network connected squirrel-cage induction generator in which the generator is linked to the turbine through the transmission. The reactive power required by the generator is provided with a mechanically switched capacitor bank.

An electronic soft starter is usually applied with these machines since they draw huge amounts of reactive current and power during low-speed operations. The operating speed of this generator varies from 1%-2%.

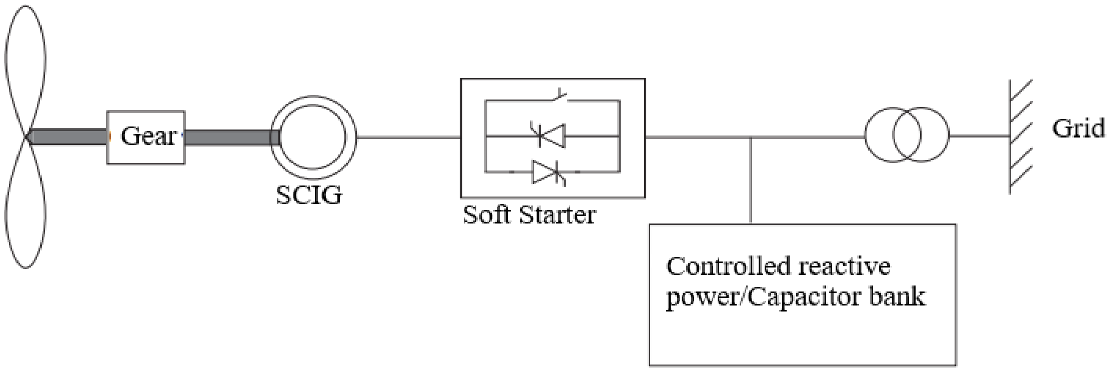

Figure 2.1: Fixed Speed WTGS (Padiyar & Kulkarni, 2019)

2.3.2. Partial Variable Speed WTGS

These are wound rotor kind induction generators (WRIG) and they are coupled directly to the power network with adjustable variable rotor resistance that allows the unit to work over a wider speed range than the previous ones. Their speed control limit is up to 10% of the synchronous speed. A soft starter can be combined to alleviate large reactive power and current devouring when the machine starts. The output electrical power of this type wind power generator is maintained nearly at rated power. Above its rated wind speed, the surplus power from the wind turbulence not controlled speedy enough by the pitch regulator is consumed as kinetic energy by changing the speed of the rotor (within 10% slip range) and dissipated as heat in the external rotor resistance as illustrated in Figure 2.2.

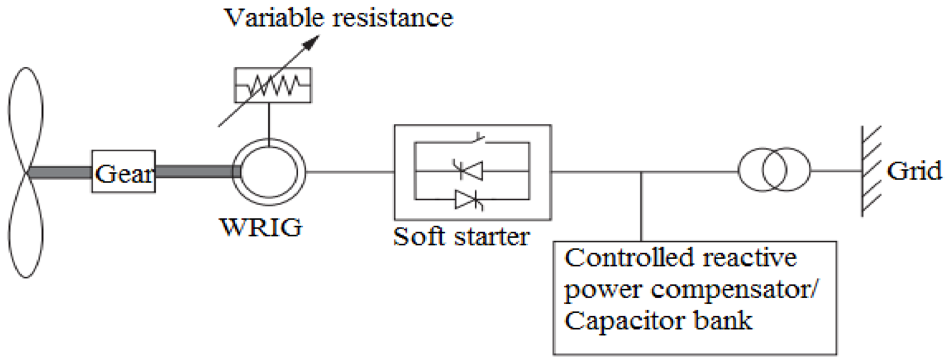

Figure 2.2: Partially Variable Speed WTGS (Padiyar & Kulkarni, 2019)

2.3.3. Partial Scale Power Converter with Variable Speed WTGS

These are DFIG-type wind powers on which their stator conductors are directly affiliated to the power network while their rotor terminals are coupled through a back-to-back PEC.

The capacity of these converters is typically about 30% of the generator rating which allows a speed variation of approximately ±30% around the synchronous speed to obtain a maximum power extraction. The power converter maintains the frequency of the rotor which makes the unit to operate at variable wind speeds. Moreover, it also controls the reactive as well as active power of the generator. Compared with the previous WTGS, the rotor energy is given into the power network by the power electronic converter instead of being dissipated as depicted in Figure 2.3.

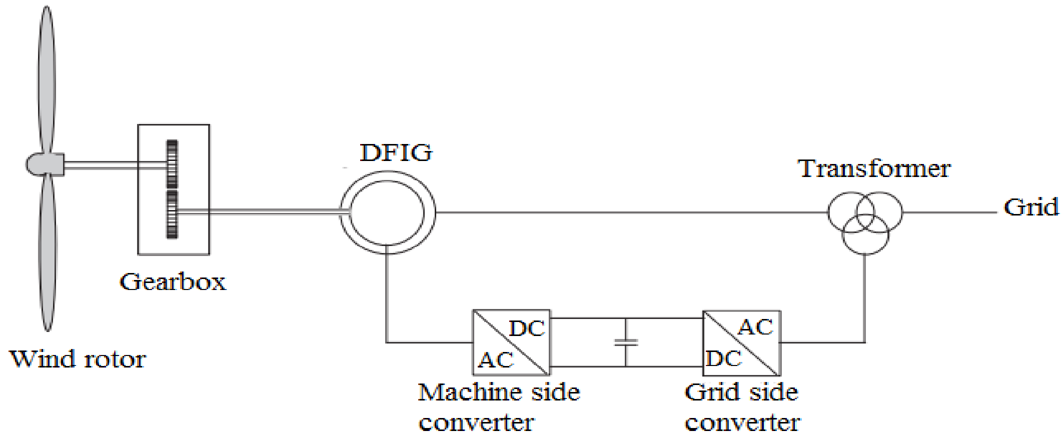

Figure 2.3: Partial Scale Power Converter with Variable Speed WTGS (Chow & Sanchez-Gasca, 2020)

2.3.4. Full-scale Power Converter with Variable Speed WTGS

In this type of arrangement, the wind power is linked to the grid via a full-rating AC-DC-AC converter as set out in Figure 2.4.

This generator can either be an induction generator (WRIG/SCIG) or a synchronous generator (WRSG/PMSG). Due to its self-excitation and transmission-free properties, a PMSG is commonly applied with full-rate converters in the wind turbine industry.

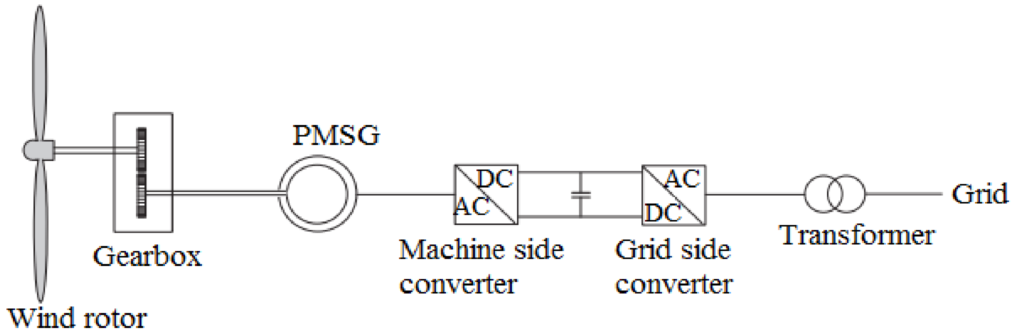

Figure 2.4: Full-Scale Power Converter with Variable Speed WTGS (Chow & Sanchez-Gasca, 2020)

2.4. Grid Code Requirements

Wind turbines are greatly influencing the system's electricity in steady as well as dynamic operation as their installation capacity is increasing rapidly. Previously, they were supposed to be disengaged under system disturbances. However, their disconnection makes it troublesome for the system to resist grid disturbances as their penetration is currently high in electric power systems. Thus, transmission system operators (TSO) have developed grid code-specified requirements for wind turbines under steady-state as well as dynamic conditions (El Archi et al., 2019).

2.4.1. Frequency and Voltage Operating Range

The wind power system needs to function within an acceptable range of the nominal voltage as well as frequency to fulfil the required demand of grid codes. Regarding of the voltage, its range could be around 10% of the nominal voltage while the frequency range for 50 Hz system may be from 49 to 51 Hz. However, the continuous frequency and voltage operating requirements of power grid varies from state to state. In the UK, for instance, the voltage range for 132 kV and 275 kV is ±10%, and for 400 kV is ±5%. The voltage allowable variation in Germany is from -12.7% to +11.8%, -12.3% to +11.4%, and -7.9% to +10.5% for 110 kV, 220 KV, and 380 kV respectively. The continuous frequency operating range in the UK is between 49.0 and 51 Hz while in Germany is from 47.5 to 51.5 Hz (Sourkounis & Tourou, 2013).

2.4.2. Active Power Control

Current grid codes need wind turbines to regulate the real power at the POI within the limited power territory.

It is maintained according to the system frequency such that the power conveyed to the power network is decreased when the grid frequency rises above the needed frequency and vice versa (Wang et al., 2019). Currently, most wind turbine generators are variable-speed ones which are regulated by power converters with speedy dynamic feedback. So, they are demanded to provide appropriate inertia to ordinary synchronous generators in which small variations in system frequency will result in the running inertias decelerating or accelerating somewhat and thereby consuming or providing surplus energy from/to the system as required by the transmission system operators (TSO).

2.4.3. Reactive Power Control

In the manner of grid codes, wind turbine generators must regulate their reactive power support or ingestion to ensure that its consumption and production are well-adjusted over the whole network. To maintain high levels of efficiency through minimising losses, power networks should work with current and voltage in phase. Usually, this specification is provided in three different ways.

- ✓ Power Factor Control: At the POI, the reactive power is maintained proportionally to the real power.
- ✓ Reactive Power Control: TSO demands independent regulation of the reactive from active power at POI.
- ✓ Voltage Control: The voltage is maintained by changing the reactive power generation in the voltage reference point.

In different grid codes, power factor as well as reactive power requirements are identical. For example, in the UK, the power factor requirement is 0.95 lagging to 0.95 leading while in Germany it is between 0.95 lagging and 0.925 leading and the requirement change depends on the voltage at the PCC (Qiuwei & Yuanzhang, 2018; Sarkar et al., 2018).

2.4.4. Low Voltage Ride Through (LVRT)

The installation of wind power is currently increasing. So, their detachment under voltage drops may result in the unbalance of the power network system and deteriorate the grid faults.

Besides to steady state operation, TSOs in various countries as shown in Figure 2.5 have published firm low-voltage ride-through (LVRT) codes for wind power plants. The capability of wind to keep coupled with the power system network during specified low-voltage situations at their POI caused by grid faults is called LVRT.

According to some power network codes, wind turbines are expected to rebuild the active power production following grid voltage recovery, and to feed a sufficient reactive current under stated low-voltage conditions.

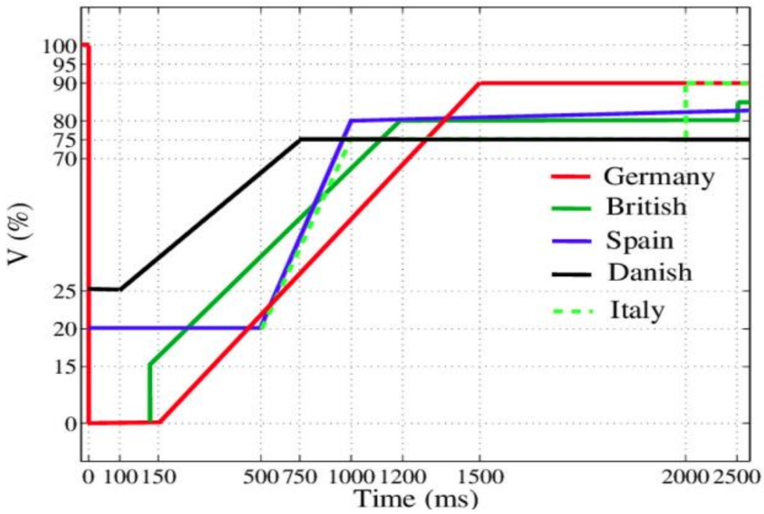

Figure 2.5: LVRT specification of different countries (Muisyo et al., 2022)

In Figure 2.5, the horizontal axis represents the withstand time, while the vertical one depicts the voltage magnitude measured at POI. The WTGs must stay united with the grid if the voltage at their POI is above the solid line. The German grid code, for instance, requires the turbine to stay attached to the power network with zero voltage magnitude for a 150-millisecond time duration and the voltage at the POI should recover to its 90% within 1500 milliseconds following the fault recovery.

2.5. DFIG Performance Under Voltage Dips

Sudden drops in the power network voltage, caused by faults such as lightning strikes, falling trees, the flow of peak currents during large motor starting, and the like between 10-90% of its rated value for a period of 0.5 cycles to 1 minute are called voltage dips/sags. The dips can be classified as symmetric and asymmetric. When all the three-phase voltages are affected by the fault in the same proportion, they are called symmetrical dips (three-phase dips). However, if the drop across each phase is different, they are referred to as asymmetrical dips (single-phase, phase-to-phase, and two-phase-to-ground dips) (Thomas & Prince, 2020).

Because of its different speed operation and minimised power converter cost, the demand for DFIG is widely increasing.

However, the direct link of its stator winding to the power network and the small power capacity of its back-to-back power electronic converter (PEC) makes it quite vulnerable to these dips. When a voltage sag is sensed at the generator terminal, the stator flux of the generator decreases, which aggravates to inrush of its stator as well as rotor currents.

This may cause damage to the stator as well as rotor circuits including, the generator stator and rotor conductors, back-to-back converters, and the DC bus fuses as well as the capacitor itself. However, the unusual change in the stator voltage needs to be compensated with a swift change in rotor voltage to avert an inrush rotor current, which is practically impossible as the capacity of the rotor circuit is around 30% of the generator rating and limiting the rotor current without control loss is not guaranteed (Mondragon Unibertsitatea, 2017). Thus, after a severe voltage dip, there is a short period at which the generator control will be lost during the evolvement of stator flux and it leads to high stator and rotor currents. So, in this project, to safeguard the generator system from overcurrent produced by the control loss and enhance its LVRT capability, fuzzy-controlled hybrid crowbar protection with SDBR is applied.

2.5.1. Crowbar

It is a protection device situated between the rotor windings of the generator and machine side power electronic converter to short circuit the transient currents induced by severe voltage drops. As laid- out in Figure 2.6, it comprises of a resistor, rectifier, and control switch, to divert the current flow through the rotor PEC. The connection/disconnection of the crowbar to the generator rotor terminal during abnormal/normal periods is controlled by the IGBT switch (Jayanthi & Devaraj, 2019).

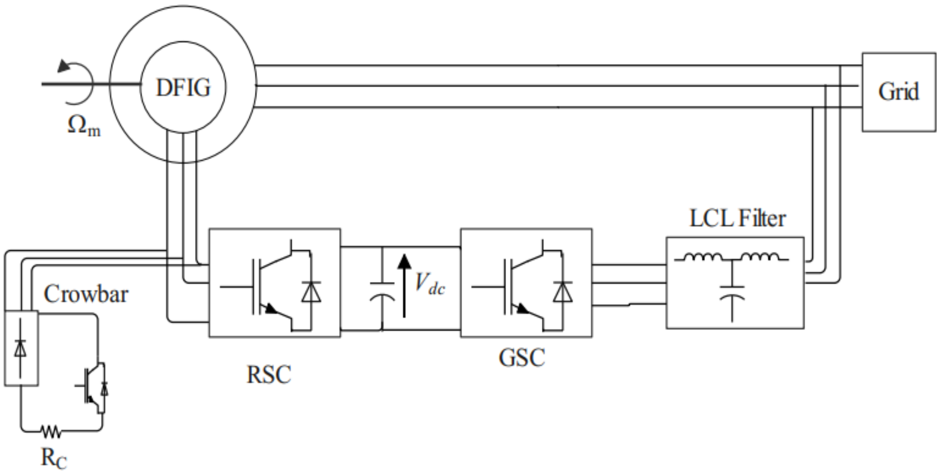

Figure 2.6: Crowbar Protection System (ABB, 2017)

The activation period of a conventional crowbar is typically 100 to 120 milliseconds (Pannell et al., 2010).

So, applying only this protection as an enhancing technique results in torque control loss and operation of the DFIG as a squirrel cage induction generator, which further worsens the mechanical stability of the machine and draws high reactive power from the grid (prolongs the dip recovery time).

2.5.2. Series Dynamic Braking Resistor (SDBR)

SDBR is a hardware-based LVRT-improving technique that adds a resistor in series to the generator stator winding to limit and increase the stator currents and voltages at the generator terminals under voltage dips respectively. It also increases the operation time of MSC, which is the crowbar-only protection weakness. As viewed in Figure 2.7, it includes a resistor with a bypass-controlled switch. This approach is preferred due to its low cost and flexible operation (Alam et al., 2018). In this paper, an IGBT switch is applied in parallel with the resistor due to its swift response and is governed by a control circuit to turn on/off in normal/ abnormal conditions so that the excessive inrush current will be damped with a parallel resistor.

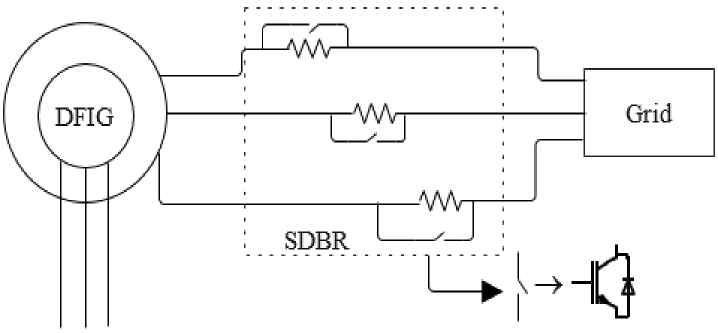

Figure 2.7: SDBR Configuration (Karkri et al., 2018)

2.5.3. Fuzzy Logic Control (FLC)

It is an artificial intelligence-based control scheme that applies the authors’ experience to solve problems. As presented in Figure 2.8, its basic structure is mainly composed of three design procedures namely fuzzifier, rule base, and de-fuzzifier (Hazari et al., 2018).

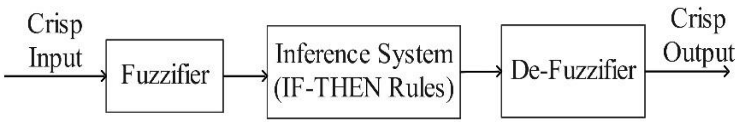

Figure 2.8: FLC Structure (Hazari et al., 2018)

The process of converting real crisp inputs/world quantities to fuzzy values with the help of membership functions is called fuzzification. These membership functions could be singleton, triangular, gaussian etc. and allocates a degree of membership between 0 to 1 for the crisp values. The fuzzy inference system relates the input and output side membership functions according to the designer's requirement in terms of IF-THEN structure. This is mainly classified as Mamdani and Sugeno-type inference systems. For decision-making, Mamdani utilises linguistic variables and fuzzy rules, while Sugeno uses mathematical functions alongside fuzzy rules. De-fuzzification is the process of transforming fuzzy sets into a crisp output value. Thus, due to computational efficiency and constant output membership function allowance Sugeno inference system is applied in this thesis work to control the IGBT switches of both the crowbar and SDBR. Moreover, a triangular membership function is taken for the input side owing to its simplicity.

CHAPTER 3

MATERIALS AND METHODS

3.1. Introduction

In this section, first, the overall methodology applied to accomplish the objective of this research work as shown in Figure 3.1 is demonstrated briefly. Then, the specific tools used to prepare this thesis document are presented shortly. Next, a mathematical modelling of the wind turbine, a DFIG, back-to-back power electronic converter, the DC-link, and the Filter are given in detail.

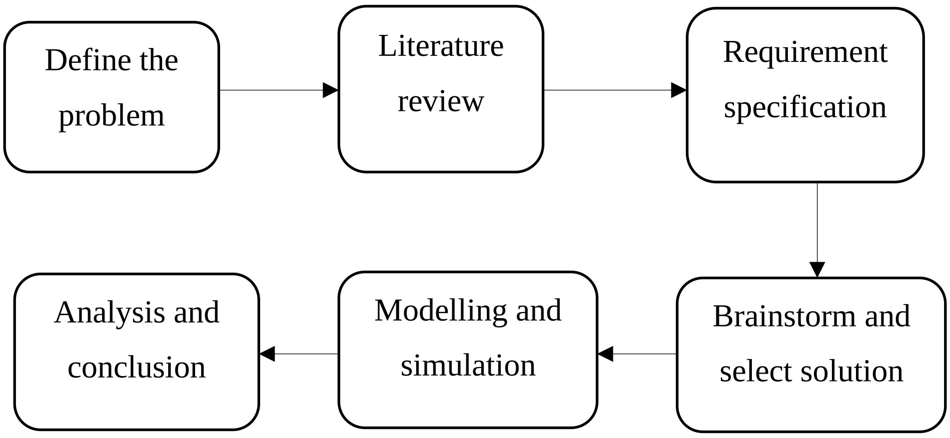

Figure 3.1: Flow Diagram of the Thesis Work

Adama II wind turbine generators are DFIG types, which need an LVRT enhancing scheme that mitigates broken of their stator as well as rotor conductor terminals, failure on their back-to-back converter IGBTs, and short circuits on their crowbar protection due to voltage dips at the grid terminal so that their availability and the stability of the grid itself will be increased. Consequently, literature on various hardware and software based low voltage ride improving techniques were reviewed. Then, initial cost, simplicity, and effective solution for the stated problem were taken as specified requirements. Following these demands, a FLC hybrid crowbar and SDBR were chosen as enhancing methods. Next, mathematical modelling of the DFIG, its power electronic converters, DC link, and Filter were done. After that, modelling and simulation of the whole system using Adama II wind power parameters in MATLAB/Simulink 2021a was accomplished. Last but not least, a meaningful analysis, interpretation, and conclusion based on the simulation results were performed.

3.2. Materials

Matlab 2021a, Edrawmax 12.0.6, Microsoft Office 2021, MathType 7.4, and Zotero 7 were the tools used to model and simulate the complete WTGS, draw figures, write this thesis paper, write mathematical equations, and add reference citations respectively.

3.3. Wind Turbine Modelling

Wind turbine captures power in kinetic form from the wind, and convert it to mechanical one with their rotor, which in further is used by a generator to produce electricity. The power of an air mass of wind (P_w) in [W], in terms of wind speed (v_w) in [m/s], area of the swept (A) in [m^2] is:

$$P_w = \frac{1}{2}\rho A {v_w}^3 = \frac{1}{2}\rho \pi R^2 {v_w}^3 \tag{3.1}$$

Where, ρ is air density in [kg/m^3], and R is the vane length in [m]. However, the wind turbine can only produce a portion of kinetic power flow into mechanical one (P_m) and is given by.

$$P_m = \frac{1}{2}\rho \pi R^2 {v_w}^3 C_P(\lambda, \theta) \tag{3.2}$$

C_P is power coefficient determined by the wind power characteristics and is related to the pitch angle (θ), and turbine tip-speed ratio (λ) as defined in equation (3.3).

$$C_P(\lambda, \theta) = 0.5176(116B_i - 0.4\theta - 5)e^{-21B_i} + 0.0068\lambda \tag{3.3}$$

$$B_i = \left(\frac{1}{\lambda + 0.08\theta} - \frac{0.035}{\theta^3 + 1}\right) \tag{3.4}$$

$$\lambda = \frac{\Omega_t R}{v_w} \tag{3.5}$$

Where, Ω_t is a rotor angular speed in [rad/s]. By Betz's limit, the highest value of C_P is theoretically 0.593. Graphically, the relation between this coefficient and the tip-speed ratio at diverse pitch angles is given in Figure 3.2.

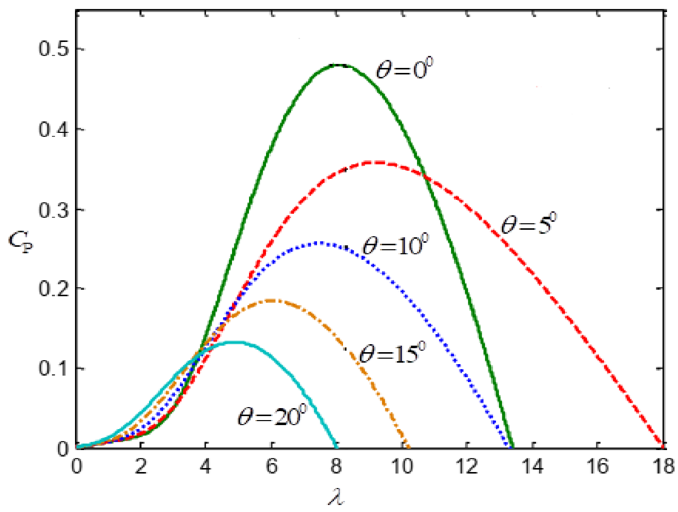

Figure 3.2: Coefficient of Power Versus Tip-Speed Ratio at Various Pitch Angles (Hazari et al., 2018)

The low-speed torque is calculated from the mechanical power gained and the rotor speed of the turbine given by:

$$T_t = \frac{P_m}{\Omega_t} \tag{3.6}$$

So, based on equations (3.2) and (3.5) the aerodynamic torque (T_t) in equation (3.6) is shown by:

$$T_t = \frac{1}{2}\rho\pi R^3 \frac{v_w^{\ 2}}{\lambda} C_P \tag{3.7}$$

The developed mechanical torque T_m input to the generator in terms of rotor torque and gearbox ratio g in expressed as

$$T_m = \frac{T_t}{g} \tag{3.8}$$

Similarly, the mechanical generator speed Ω_m as a in terms of rotor speed of the rotor and the transmission ratio is calculated by

$$\Omega_m = g\Omega_t \tag{3.9}$$

Dynamically, the shaft that connects with its low speed the gearbox to the turbine and with its high speed to the generator can be modelled in first order differential equation as presented in (3.10).

$$T_m - T_{em} - D\Omega_t = J\frac{d\Omega_m}{dt} \tag{3.10}$$

Where, T_{em}, D, and J stands for the generator torque in [Nm], damping coefficient, and the total system inertia in [kg.m^2].

3.3.1. Maximum Power Point Tracking (MPPT)

This tracker is devoted to regulate the machine side power electronic converter by tracking the optimum torque reference value to maximise the efficiency of the turbine via fixing an optimal value of tip-speed ratio and the maximum coefficient of power. In this study, an indirect speed control is used to control the rotation speed indirectly by operating at $\lambda = \lambda_{opt}$, and $C_P = C_{P\max}$ (El-Jalyly et al., 2019; Zgarni & El Amraoui, 2022).

So, putting the expression of v_w in equation (3.5) into (3.2) and replacing the tip speed ratio and coefficient of power with their optimum values will outcomes in optimum power P_{opt} as

$$P_{opt} = \frac{1}{2}\rho\pi\frac{R^5}{\lambda_{opt}^3}C_{P\max}\Omega_t^3 \tag{3.11}$$

Thus, applying equation (3.9) and (3.11) results in

$$P_{opt} = \frac{1}{2}\rho\pi\frac{R^5}{\lambda_{opt}^3}C_{P\max}\left(\frac{\Omega_m}{g}\right)^3 \tag{3.12}$$

3.4. DFIG Modelling

Modelling of DFIG is a key to design the control system for these wind turbine generators as their model describes the operation relationship of its variables and to carry out various analysis. Primarily, the DFIG will be modelled in the steady condition to figure out the performance of the generator in a steady state. Then, the DFIG and back-to-back PEC will be modelled in different reference frames dynamically.

3.4.1. Steady State Model of DFIG

To perform this model, the following assumptions need to be considered.

- ✓ The power network supplies uniform three phase voltages with stable magnitude and frequency for the stator.

- ✓ The rotor winding is also fed at fixed and balanced AC voltage magnitude and frequency separately from the stator by a back-to-back PEC.
- ✓ Both the rotor and stator windings are configured in star connection.
- ✓ Only a single phase of the stator and rotor is modelled since the three-phase windings of DFIGs are symmetrical and balanced in structure.

Figure 3.3 represents a phase steady-state equivalent circuit of DFIG.

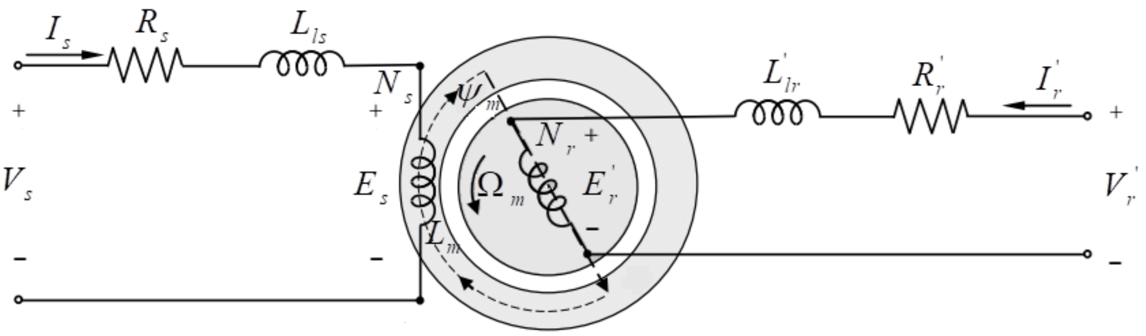

Figure 3.3: Steady-State Equivalent Circuit of One-Phase DFIG (Abad et al., 2011b)

Before proceeding to the study of the electric equations of the DFIG, knowing the relationships between different frequencies of the machine is necessary. The rotor shaft spins a mechanical speed of, Ω_m . For a pole pair p of the DFIG, the electrical frequency of the rotor shaft ω_m is given by

$$p\Omega_m = \omega_m \tag{3.13}$$

The angular current as well as voltage frequency of the stator windings $\omega_s = 2\pi f_s$ is constant since the stator part of the DFIG is linked to the power network. Where, f_s is the power network frequency. The angular frequency of voltages as well as currents in the rotor windings ω_r rely on both the stator currents and voltages frequency ω_s and rotor electrical speed ω_m. It is also known as the angular frequency of the slip of the generator and is expressed as

$$\omega_r + \omega_m = \omega_s \tag{3.14}$$

The machine's slip s is calculated as

$$s = \frac{\omega_r}{\omega_s} \tag{3.15}$$

The slip frequency f_r is also derived as $L_{lr}^{'}$

$$f_r = \frac{\omega_r}{2\pi} \tag{3.16}$$

Using Figure 3.3, the stator and rotor side phasor equations of the DFIG correspondingly are

$$V_s = E_s + \left(R_s + j\omega_s L_{ls}\right) I_s \tag{3.17}$$

$$V_r^{'} = E_r^{'} + \left(R_r^{'} + j\omega_r L_{lr}^{'}\right) I_r^{'} \tag{3.18}$$

Where, V_s and $V_r^{'}$ are the stator and rotor phase voltages supplied by the grid and the converter, respectively. E_s and $E_r^{'}$, illustrates induced stator as well as rotor electromotive forces. R_s and $R_r^{'}$, indicates the resistances of stator as well as rotor. I_s and $I_r^{'}$ presents the phase currents of the stator and rotor. L_{ls} and $L_{lr}^{'}$ are the stator and rotor winding leakage inductances.

To comprehend the relationship among the stator and rotor variables, it is routine to convert the rotor side electrical variables into the stator side.

The mutual flux ψ_m couples the DFIG stator and rotor windings. The generated emf on the stator winding is stated as

$$E_s = j\omega_s k_s N_s \psi_m \tag{3.19}$$

Where k_s and N_s are the stator winding factor and per phase turn number respectively. In the same manner, the induced rotor winding emf is expressed as

$$E_r^{'} = j\omega_r k_r N_r \psi_m \tag{3.20}$$

Where k_r and N_r are the rotor winding factor and per phase turns respectively. From equations (3.19) and (3.20), the relation between E_s and $E_r^{'}$ is represented as

$$\frac{E_r^{'}}{E_s^{'}} = \frac{\omega_r k_r N_r}{\omega_s k_s N_s} \approx s\frac{1}{u} \tag{3.21}$$

Where $\frac{N_s}{N_r} = u$ and $\frac{k_r}{k_s} \approx 1$.

After substituting equation (3.21) to (3.18) the following equation is derived.

$$V_r^{'} = s\frac{E_s}{u} + \left(R_r^{'} + j\omega_r L_{lr}^{'}\right) I_r^{'} \tag{3.22}$$

Multiplying both sides of equation (3.22) by $\frac{u}{s}$ yields

$$\frac{u}{s}V_r^{'} = E_s + \left(\frac{u^2}{s}R_r^{'} + j\omega_s u^2 L_{lr}^{'}\right)\frac{I_r^{'}}{u} \tag{3.23}$$

To facilitate the analysis, transforming the rotor variables to the stator side similar to the transformer is natural through the following equivalences.

$$uV_r^{'} = V_r \tag{3.24}$$

$$\frac{I_r^{'}}{u} = I_r \tag{3.25}$$

$$u^2 R_r^{'} = R_r \tag{3.26}$$

$$u^2 L_{lr}^{'} = L_{lr} \tag{3.27}$$

Where, V_r, I_r, R_r, and L_{lr} represents the rotor voltage in [V], current in [A], resistance in [Ω], and leakage inductance in [H] referred to the stator side respectively. Applying equations (3.24) and (3.27), equation (3.23) becomes

$$\frac{V_r}{s} = E_s + \left(\frac{R_r}{s} + j\omega_s L_{lr}\right) I_r \tag{3.28}$$

The induced emf in the stator, E_s produces a magnetic current I_m through the magnetizing inductance L_m and their relation is shown in equation (3.29).

$$E_s = j\omega_s L_m \mathrm{I_m} \tag{3.29}$$

Joining equations (3.19) and (3.29) produces

$$\psi_m = L_m \mathrm{I_m} \tag{3.30}$$

So, by changing the rotor parameters to the stator sides, the single-phase steady state equivalent circuit of the DFIG where all magnitudes are in the same frequency is drawn in Figure 3.4.

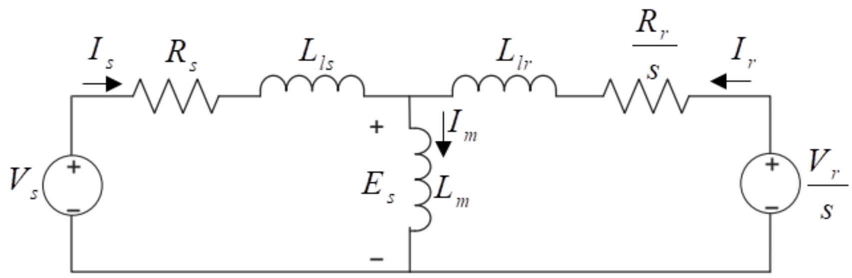

Figure 3.4: Stator Referred Single Phase Equivalent Circuit of Steady State DFIG (D. Xu et al., 2018)

Based on the currents, the stator flux ψ_s and rotor flux ψ_r are derived using the following expressions.

$$\psi_s = L_{ls} I_s + L_m \left(I_s + I_r \right) = L_m I_r + L_s I_s \tag{3.31}$$

$$\psi_r = L_{lr} I_r + L_m \left(I_s + I_r \right) = L_m I_s + L_r I_r \tag{3.32}$$

Where $L_m + L_{ls} = L_s$ and $L_m + L_{lr} = L_r$ are the stator as well as rotor inductances.

Applying KCL to Figure 3.4 provides

$$I_s + I_r = I_m \tag{3.33}$$

So, using the flux expressions from (3.31) and (3.32) into (3.17) and (3.28), the flux-related voltages referred to the stator side are given as

$$V_s = R_s I_s + j\omega_s \psi_s \tag{3.34}$$

$$V_r = R_r I_r + js\omega_s \psi_r \tag{3.35}$$

3.4.1.1. DFIG Power and Torque Expressions

i) Active Power Expression

Analysing the power relations of the DFIG is imperative to study its different modes of operation. So, based on the driven equivalent circuit, the basic active power expression is given provided as follows.

Using KVL to the left-hand hoop of Figure 3.4 gives

$$-V_s + \left(R_s + jX_{ls} \right) I_s + jX_m I_m = 0 \tag{3.36}$$

Where $X_m = \omega_s L_m$ and $X_{ls} = \omega_s L_{ls}$.

In the same way, applying KVL to the right-side loop of Figure 3.4 results in

$$\frac{-V_r}{s} + \left(\frac{R_r}{s} + jX_{lr}\right) I_r + jX_m I_m = 0 \tag{3.37}$$

Where $X_{lr} = \omega_s L_{lr}$

The per-phase power in the rotor is defined as

$$P_r = \mathrm{Re}\left\{V_r I_r^*\right\} \tag{3.38}$$

Where P_r and the superscript "*" indicates for the rotor power and complex conjugate respectively.

Inserting V_r equation of (3.37) in to (3.38) and considering $I_r I_r^* = I_r^2$ results in

$$P_r = \mathrm{Re}\left\{R_r I_r I_r^* + jsX_m I_m I_r^* + jsX_{lr} I_r I_r^*\right\} = R_r I_r^2 + \mathrm{Re}\left\{jsX_m I_m I_r^*\right\} \tag{3.39}$$

By applying the I_r equivalence from equation (3.33) to (3.39) and remembering $\mathrm{Re}\left\{jsX_m I_m I_m^*\right\} = 0$, the power flow through the rotor is computed by

$$P_r = R_r I_r^2 + \mathrm{Re}\left\{jsX_m I_m \left(I_m^* - I_s^*\right)\right\} = R_r I_r^2 + \mathrm{Re}\left\{jsX_m I_m \left(-I_s^*\right)\right\} \tag{3.40}$$

Substituting the expression of $X_m I_m$ from equation (3.36) in to (3.40) yields

$$P_r = R_r I_r^2 + s\,\mathrm{Re}\left\{\left(V_s - R_s I_s + jX_{ls} I_s\right)\left(-I_s^*\right)\right\} = R_r I_r^2 + sR_s I_s^2 - s\,\mathrm{Re}\left\{V_s I_s^*\right\} \tag{3.41}$$

The per-phase stator active power is also shown by

$$P_s = \mathrm{Re}\left\{V_s I_s^*\right\} \tag{3.42}$$

Putting equation (3.42) into (3.41) results in

$$P_r = -sP_s + sR_s I_s^2 + R_r I_r^2 \tag{3.43}$$

On the other hand, equation (3.43) can be represented as

$$P_r = s\left(P_{cu\_s} - P_s\right) + P_{cu\_r} \tag{3.44}$$

Where $P_{cu\_r} = R_r I_r^2$ and $P_{cu\_s} = R_s I_s^2$ stands for the rotor as well as stator winding copper losses of the machine respectively. As these copper losses are negligible compared to both the stator as well as rotor power flows, neglecting them and considering equation (3.44) yields

$$P_r \approx -sP_s \tag{3.45}$$

According to slip ratio s, it is noticed that P_r is a portion of P_s. Basically, -30% to 30% is the range of wind turbine slip ratio s. So, the rotor PEC can control the stator power.

Thus, as shown in Figure 3.5, the total flow of power, P to grid can be stated by

$$P_s + P_r = P \tag{3.46}$$

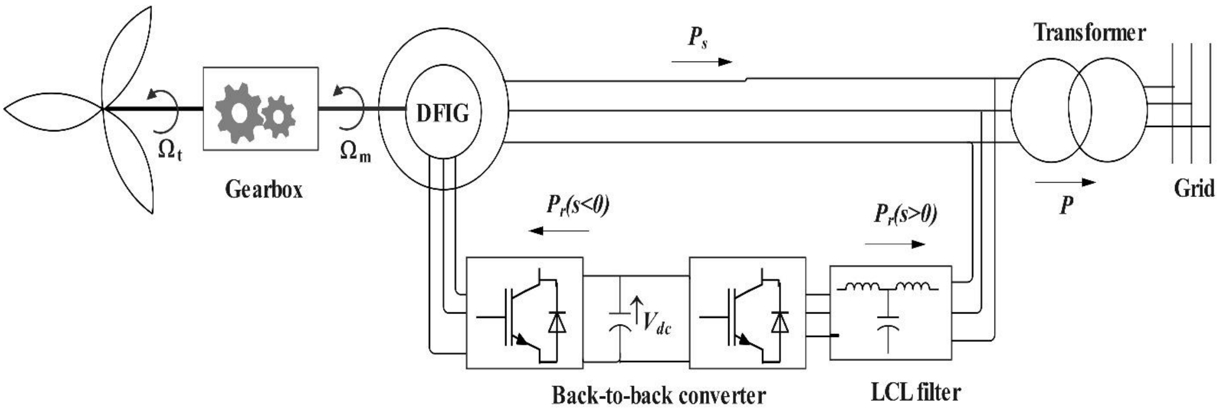

Figure 3.5: Power Flow in DFIG Wind Turbines (ABB, 2017)

Applying the P_r relation in equation (3.45), the total power P is given by

$$P = -sP_s + P_s = P_s(1-s) \tag{3.47}$$

Based on rotor speed, the DFIG wind power has three modes of operation.

- ✓ Sub/hypo-synchronous mode
- ✓ Synchronous mode and
- ✓ Super/hyper-synchronous mode

During hypo-synchronous, the synchronous angular frequency ω_s is greater than the rotor angular frequency ω_m so that slip $s > 0$.

In this mode of operation, the rotor takes power from the power network while the stator feeds power to it. Referring to equation (3.47), the overall power flow to the power network is $P = P_s\left(1-|s|\right)$.

In the synchronous mode of operation, the synchronous angular frequency is identical to the rotor angular frequency (i.e., $s = 0$) and only the stator provides power to the network. The rotor winding receives DC current flows and the complete power flow to the power network based on equation (3.47) is $P = P_s$.

On the other hand, the synchronous angular frequency ω_s is less than the rotor angular frequency ω_m and slip $s < 0$ in hyper synchronous mode of operation. The power is supplied to the network through the stator and rotor circuits. Thus, the total power delivered to the grid using equation (3.47) is $P = P_s\left(1+|s|\right)$.

ii) Reactive Power Expression

In the same way, the reactive power expressions are derived as follows.

The per-phase rotor reactive power Q_r similar to equation (3.38) is represented by

$$Q_r = \mathrm{Im}\left(V_r I_r^*\right) \tag{3.48}$$

Replacing V_r from equation (3.37) and noticing that $I_r I_r^* = I_r^2$, the reactive power flow through the rotor is derived as

$$Q_r = \mathrm{Im}\left\{R_r I_r I_r^* + jsX_m I_m I_r^* + jsX_{lr} I_r I_r^*\right\} = sX_{lr} I_r^2 + \mathrm{Im}\left\{jsX_m I_m I_r^*\right\} \tag{3.49}$$

Substituting equation (3.33) in to (3.49) and remarking that $I_m I_m^* = I_m^2$ yields

$$Q_r = sX_{lr} I_r^2 + \mathrm{Im}\left\{jsX_m I_m\left(I_m^* - I_s^*\right)\right\} = sX_m I_m^2 + sX_{lr} I_r^2 - \mathrm{Im}\left\{jsX_m I_m I_s^*\right\} \tag{3.50}$$

Similarly, expressing the term $X_m I_m$ from equation (3.36) into (3.50) gives

$$Q_r = sX_m I_m^2 + sX_{lr} I_r^2 - \mathrm{Im}\left\{s\left(V_s - R_s I_s - jX_{ls} I_s\right) I_s^*\right\} \tag{3.51}$$

Bearing in mind that $I_s I_s^* = I_s^2$ and placing it in equation (3.51) provides

$$Q_r = sX_m I_m^2 + sX_{lr} I_r^2 + sX_{ls} I_s^2 - s\,\mathrm{Im}\left\{V_s I_s^*\right\} \tag{3.52}$$

The per-phase stator reactive power Q_s is stated by

$$Q_s = \mathrm{Im}\left\{V_s I_s^*\right\} \tag{3.53}$$

So, equation (3.52) can be expressed as

$$Q_r = sX_m I_m^2 + sX_{lr} I_r^2 + sX_{ls} I_s^2 - sQ_s \tag{3.54}$$

Moreover, equation (3.54) can be written as

$$Q_r = s(Q_m + Q_{lr} + Q_{ls} - Q_s) \tag{3.55}$$

Where $Q_{lr} = X_{lr} I_r^2$ stands for leakage inductive reactive power, $Q_m = X_m I_m^2$ is the reactive power of magnetising inductance, and $Q_{ls} = X_{ls} I_s^2$ is the reactive power of stator leakage inductance.

As the stator reactive power is much greater than the reactive power due to the mutual, stator and rotor leakage inductances, equation (3.55) can be estimated as

$$Q_r = -sQ_s \tag{3.56}$$

iii) Torque Expression

The per-phase electromagnetic torque T_{em} in terms of stator active power P_s synchronous angular frequency ω_s, and number of pole pairs p can be defined as (Abad et al., 2011b; Abu-Rub et al., 2014).

$$T_{em} = \frac{pP_s}{\omega_s} \tag{3.57}$$

Substituting equation (3.42) into (3.57) and neglecting the resistive power loss yields

$$T_{em} = \frac{p}{\omega_s}\left(\mathrm{Re}\{ j\omega_s L_m I_r I_s^*\right) \tag{3.58}$$

Combining expressions (3.31) and (3.58) provides

$$T_{em} = p\,\mathrm{Im}\{\psi_s^* I_s) \tag{3.59}$$

3.4.2. Dynamic Model of DFIG

This model is required for the dynamic analysis and control system design of the machine. It assists in knowing the continuous characteristics of machine variables, for instance, flux, torque, and currents under certain voltage-providing situations. These variables describe the behaviour of the machine. However, as these variables are time-varying and nonlinear, their modelling is complicated. So, to reduce three-phase modelling complications, the three windings of the stator as well as the rotor are represented in two phases using space vector theory as pictured in Figure 3.6. To cultivate the space vector model of the DFIG, three various rotating reference frames, namely, the stator $(\alpha\beta)$, the rotor (DQ), and the synchronous reference frames (dq) are employed. The following assumptions are initiated to simplify the dynamic analysis.

- ✓ The stator and rotor core losses are ignored.
- ✓ The stator as well as rotor core magnetic saturation are ignored.
- ✓ The stator along with the rotor windings are independent of the temperature and frequency.
- ✓ Each winding of the generator is symmetrical.

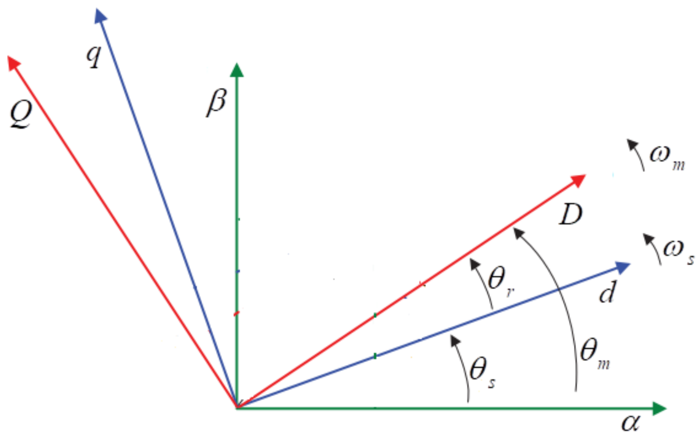

Figure 3.6: Space Vector Representation of Different Reference Frames (Tuka, 2020)

3.4.2.1. αβ Model

Each stator as well as rotor phase coils of a DFIG can be represented in space vector form as shown in equations (3.60) and (3.61) individually.

$$V_s = \frac{d\psi_s}{dt} + R_s i_s \tag{3.60}$$

$$V_r = \frac{d\psi_r}{dt} + R_r i_r \tag{3.61}$$

Where R_s, i_s, V_s, and ψ_s are the stator resistance in [Ω], current in [A], voltage in [V],and flux space vectors in [Wb] respectively. V_r, R_r, i_r, and ψ_r are the rotor voltage in [V], resistance in [Ω], current in [A], and flux space vectors in [Wb]. To represent the voltage relations in $(\alpha\beta)$ reference frame, the rotor equation given in expression (3.61) needs to be multiplied with $e^{j\theta m}$, which results in the subsequent equivalences.

$$\frac{d\psi_{\alpha s}}{dt} + R_s i_{\alpha s} = V_{\alpha s} \tag{3.62}$$

$$\frac{d\psi_{\beta s}}{dt} + R_s i_{\beta s} = V_{\beta s} \tag{3.63}$$

$$\frac{d\psi_{\alpha r}}{dt} + R_r i_{\alpha r} + \psi_{\beta r}\omega_m = V_{\alpha r} \tag{3.64}$$

$$\frac{d\psi_{\beta r}}{dt} + R_r i_{\beta r} - \psi_{\alpha r}\omega_m = V_{\beta r} \tag{3.65}$$

Where, $i_{\alpha s}$, $i_{\alpha r}$, $V_{\alpha s}$, $V_{\alpha r}$, $\psi_{\alpha s}$, $\psi_{\alpha r}$, and $i_{\beta s}$, $i_{\beta r}$, $V_{\beta s}$, $V_{\beta r}$, $\psi_{\beta s}$, $\psi_{\beta r}$ are the stator and rotor currents in [A], voltages in [V], and fluxes in [Wb] in $\alpha\beta$ axis respectively.

Similarly, the stator as well as rotor flux space vector equations in $(\alpha\beta)$ reference frame applying equations (3.31) and (3.32) are stated by

$$\psi_{\alpha s} = L_m i_{\alpha s} + L_s i_{\alpha s} \tag{3.66}$$

$$\psi_{\beta s} = L_m i_{\beta s} + L_s i_{\beta s} \tag{3.67}$$

$$L_m i_{\alpha r} + L_r i_{\alpha r} = \psi_{\alpha r} \tag{3.68}$$

$$L_m i_{\beta r} + L_r i_{\beta r} = \psi_{\beta r} \tag{3.69}$$

Where, L_r, L_s, and L_m are the rotor, stator, and mutual inductances in [H].

The DFIG stator and rotor side reactive as well as active powers in $\alpha\beta$ reference frames are computed by

$$P_s = 1.5\,\mathrm{Re}\left\{V_s i_s^*\right\} = 1.5\left(i_{\alpha s}V_{\alpha s} + i_{\beta s}V_{\beta s}\right) \tag{3.70}$$

$$Q_s = 1.5\,\mathrm{Im}\left\{V_s i_s^*\right\} = 1.5\left(i_{\alpha s}V_{\beta s} - i_{\beta s}V_{\alpha s}\right) \tag{3.71}$$

$$P_r = 1.5\,\mathrm{Re}\left\{V_r i_r^*\right\} = 1.5\left(i_{\alpha r}V_{\alpha r} + i_{\beta r}V_{\beta r}\right) \tag{3.72}$$

$$Q_r = 1.5\,\mathrm{Im}\left\{V_r i_r^*\right\} = 1.5\left(i_{\alpha r}V_{\beta r} - i_{\beta r}V_{\alpha r}\right) \tag{3.73}$$

Where the superscript * stands for a complex conjugate. P_s, P_r, Q_s, and Q_r represents the stator and rotor real powers in [W], as well as reactive powers in [VA] respectively.

The electromagnetic torque developed T_{em} by the DFIG is derived as

$$T_{em} = 1.5p\,\mathrm{Im}\left(\psi_r I_r^*\right) = 1.5p\left(\psi_{\beta r} i_{\alpha r} - \psi_{\alpha r} i_{\beta r}\right) \tag{3.74}$$

Alternatively, the electromagnetic torque applying equations (3.66) to (3.69) and (3.74) can also be expressed as

$$T_{em} = \frac{3}{2}p\frac{L_m}{mL_sL_r}\left(\psi_{\alpha r}\psi_{\beta s} - \psi_{\beta r}\psi_{\alpha s}\right) = \frac{3}{2}p\frac{L_m}{mL_sL_r}\mathrm{Im}\left(\psi_r^*\psi_s\right) \tag{3.75}$$

Where, $m = \dfrac{L_rL_s - L_m^2}{L_rL_s}$ is a leakage coefficient.

Where p indicates the machine pole pairs.

Thus, the dynamic model equivalent circuits in $\alpha\beta$ reference frame of the DFIG are revealed in Figures 3.7 and 3.8 below.

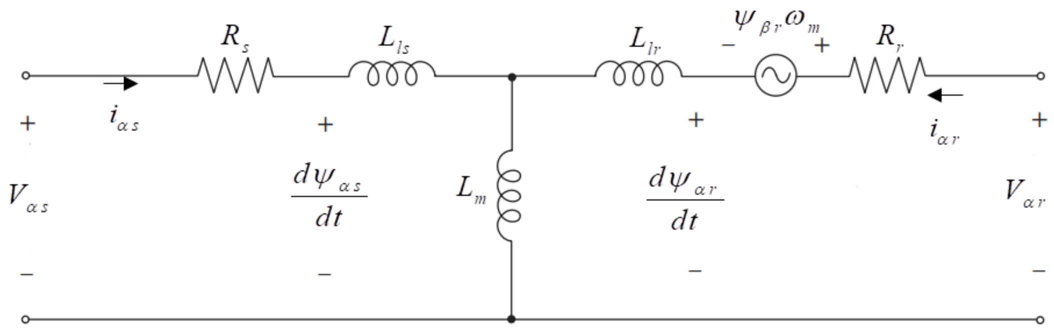

Figure 3.7: DFIG Equivalent Circuit in α-axis (Zgarni & El Amraoui, 2022)

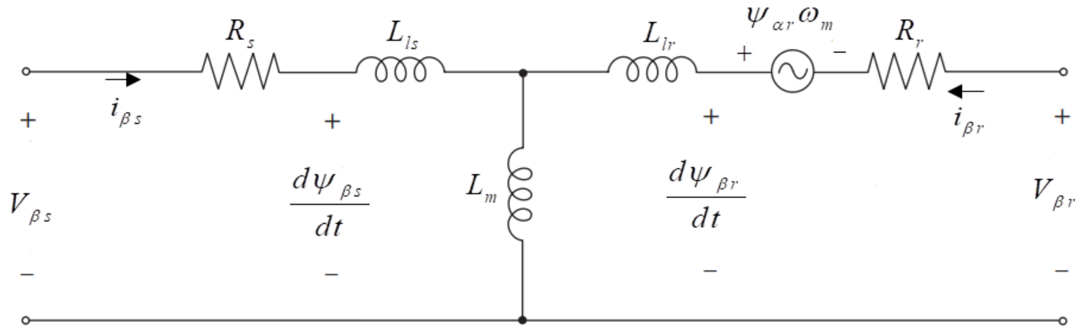

Figure 3.8: DFIG Equivalent Circuit in β-axis (Zgarni & El Amraoui, 2022)

3.4.2.2. dq Model

In the synchronous reference frame (dq),the differential equations that represents the model of the DFIG are derived by multiplying equations (3.60) and (3.61) with $e^{-j\theta_s}$ and $e^{-j\theta_r}$ respectively as stated in the following set of equations.

$$V_{ds} = \frac{d\psi_{ds}}{dt} + R_s i_{ds} - \psi_{qs}\omega_s \tag{3.76}$$

$$V_{qs} = \frac{d\psi_{qs}}{dt} + R_s i_{qs} + \psi_{ds}\omega_s \tag{3.77}$$

$$V_{dr} = \frac{d\psi_{dr}}{dt} + R_r i_{dr} - \psi_{qr}\omega_r \tag{3.78}$$

$$V_{qr} = \frac{d\psi_{qr}}{dt} + R_r i_{qr} + \psi_{dr}\omega_r \tag{3.79}$$

V_{ds}, V_{dr}, i_{ds}, i_{dr}, ψ_{ds}, ψ_{dr}, and V_{qs}, V_{qr}, i_{qs}, i_{qr}, ψ_{qs}, ψ_{qr} denotes the voltages in [V], currents in [A], and fluxes in [Wb] of the stator as well as rotor in dq axis respectively.

In the same way, the flux equations from equations (3.31) and (3.32) are derived as

$$\psi_{ds} = L_m i_{dr} + L_s i_{ds} \tag{3.80}$$

$$\psi_{qs} = L_m i_{qr} + L_s i_{qs} \tag{3.81}$$

$$L_m i_{ds} + L_r i_{dr} = \psi_{dr} \tag{3.82}$$

$$L_m i_{qs} + L_r i_{qr} = \psi_{qr} \tag{3.83}$$

The power and torque expressions in dq reference frames are the same with $\alpha\beta$ equations as derived below.

$$P_s = 1.5\,\mathrm{Re}\left\{V_s i_s^*\right\} = 1.5\left(i_{ds}V_{ds} + i_{qs}V_{qs}\right) \tag{3.84}$$

$$P_r = 1.5\,\mathrm{Re}\left\{V_r i_r^*\right\} = 1.5\left(i_{dr}V_{dr} + i_{qr}V_{qr}\right) \tag{3.85}$$

$$Q_s = 1.5\,\mathrm{Im}\left\{V_s i_s^*\right\} = 1.5\left(i_{ds}V_{qs} - i_{qs}V_{ds}\right) \tag{3.86}$$

$$Q_r = 1.5\,\mathrm{Im}\left\{V_r i_r^*\right\} = 1.5\left(i_{dr}V_{qr} - i_{qr}V_{dr}\right) \tag{3.87}$$

The torque is also given by

$$T_{em} = 1.5p\,\mathrm{Im}\left(\psi_r I_r^*\right) = 1.5p\left(\psi_{qr}i_{dr} - \psi_{dr}i_{qr}\right) \tag{3.88}$$

So, based on the developed dq reference equations, the dynamic model equivalent circuit in a synchronously rotating frame is presented in Figures 3.9 as well as 3.10 below.

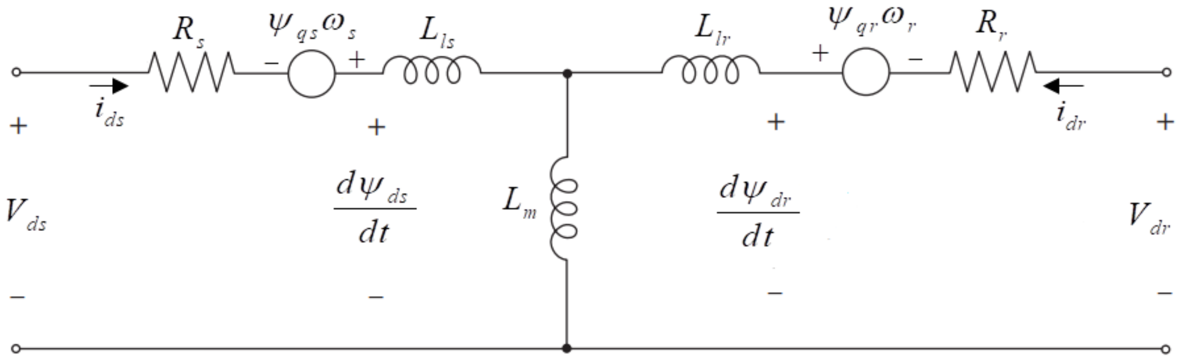

Figure 3.9:DFIG Equivalent Circuit in d-axis (Elgbaily et al., 2022)

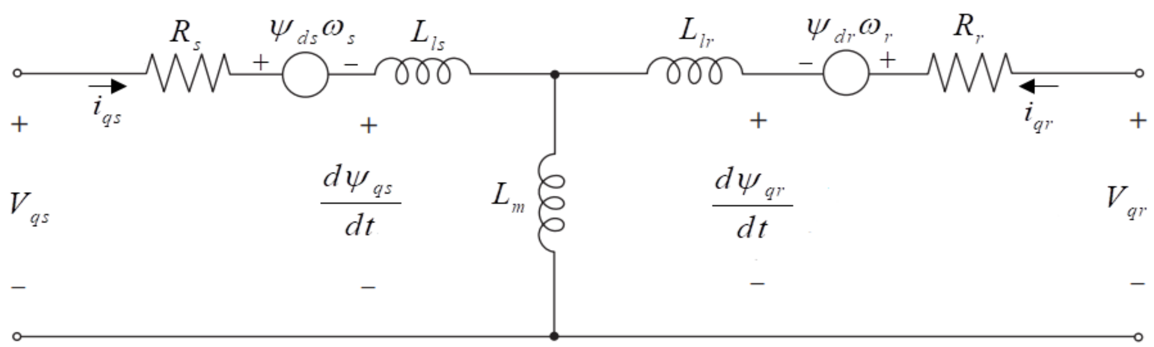

Figure 3.10: DFIG Equivalent Circuit in q-axis (Elgbaily et al., 2022)

3.5. Power Converter Modelling

Due to their quick and accurate responses, PECs are hugely applicable in adjustable speed drives. They are used in different operation speed WTGS, such as DFIG-type WECS to regulate the generator's torque and voltage. Variable speed wind turbine generators mainly utilise back-to-back with IGBT type voltage source converters.

Even though there are different three phase back to back converter configurations, a two-level voltage source converter (VSC) is the most commonly used for low or medium-power purposes (Vozikis et al., 2020).

3.5.1. Machine Side Converter (MSC) Model

The MSC is located between the generator rotor winding and the DC link busbar. It operates as an inverter or rectifier according to the rotor speed. In hypo-synchronous speed, it works as an inverter. On the other hand, it performs as a rectifier in hyper-synchronous cases. This converter maintains the rotor flux and torque of the generator. Regulating the flow of reactive power is also one of its mandates. This VSC has eight switching patterns and produces eight probable voltage vectors.

As exposed in Figure 3.11, the corresponding rotor converter output voltages are created by commanding the suitable switching sequences of the IGBTs.

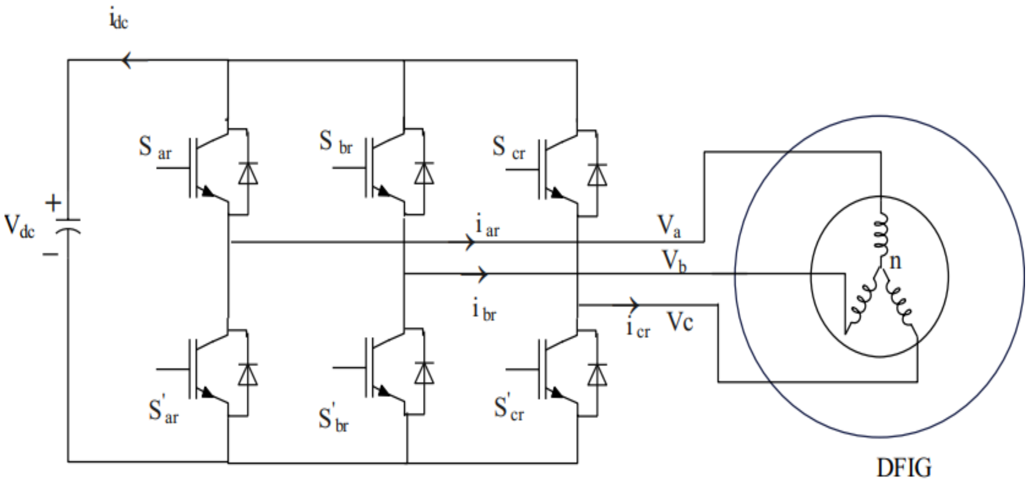

Figure 3.11: Power Circuit of Machine Side Converter (MSC) (Vozikis et al., 2020)

So, the converted three-phase output voltages from the DC bus are modelled as

$$\begin{pmatrix} V_{an} \\ V_{bn} \\ V_{cn} \end{pmatrix} = \frac{V_{dc}}{3} \begin{pmatrix} 2 & -1 & -1 \\ -1 & 2 & -1 \\ -1 & -1 & 2 \end{pmatrix} \begin{pmatrix} S_{ar} \\ S_{br} \\ S_{cr} \end{pmatrix} \quad (3.89)$$

Where, V_{an} , V_{bn} ,V_{cn}, V_{dc} , and S_{ar} , S_{br} , S_{cr} expresses the rotor output ac phase to neutral voltages in [V], DC bus voltage in [V], and the upper IGBT switch positions of the MSC respectively. Ideally, the upper and lower IGBT switches are a complement to each other.

Moreover, the output voltages described in equation (3.89) can be denoted in space vector form as shown in Appendix B using Clarke transformation by

$$V_k = v_\alpha + jv_\beta = \frac{2}{3}\left[V_{an} + aV_{bn} + a^2V_{cn}\right] \tag{3.90}$$

Where, V_k is the resultant voltage vector from $k = 0,...,7$, v_α and v_β are the α and β axis space vectors, and $a = e^{j\frac{2\pi}{3}}$ is an operator.

Based on the eight possible switching states of S_{ar} , S_{br} , S_{cr} , the eight various output voltage combinations with their corresponding space vector values are shown in Table 3.1 below.

Table 3.1: Eight Output Voltage Combinations of a Two-Level VSC

S_{ar}	S_{br}	S_{cr}	V_{an}	V_{bn}	V_{cn}	v_α	v_β	Vector symbol
0	0	0	0	0	0	0	0	V_0
1	0	0	$\frac{2}{3}V_{dc}$	$\frac{-1}{3}V_{dc}$	$\frac{-1}{3}V_{dc}$	$\frac{2}{3}V_{dc}$	0	V_1
1	1	0	$\frac{1}{3}V_{dc}$	$\frac{1}{3}V_{dc}$	$\frac{-2}{3}V_{dc}$	$\frac{V_{dc}}{3}$	$\frac{1}{\sqrt{3}}V_{dc}$	V_2
0	1	0	$\frac{-1}{3}V_{dc}$	$\frac{2}{3}V_{dc}$	$\frac{-1}{3}V_{dc}$	$\frac{-1}{3}V_{dc}$	$\frac{1}{\sqrt{3}}V_{dc}$	V_3
0	1	1	$\frac{-2}{3}V_{dc}$	$\frac{1}{3}V_{dc}$	$\frac{1}{3}V_{dc}$	$\frac{-2}{3}V_{dc}$	0	V_4
0	0	1	$\frac{-1}{3}V_{dc}$	$\frac{-1}{3}V_{dc}$	$\frac{2}{3}V_{dc}$	$\frac{-1}{3}V_{dc}$	$\frac{-1}{\sqrt{3}}V_{dc}$	V_5
1	0	1	$\frac{1}{3}V_{dc}$	$\frac{-2}{3}V_{dc}$	$\frac{1}{3}V_{dc}$	$\frac{1}{3}V_{dc}$	$\frac{-1}{\sqrt{3}}V_{dc}$	V_6
1	1	1	0	0	0	0	0	V_7

The eight possible combinations in the space vector diagram using Table 3.1 are drawn in Figure 3.12. From these resultant voltages, V_0 and V_1 are known as zero-vectors while $V_1,...,V_6$ active vectors and they are displaced by 60^o phase shit.

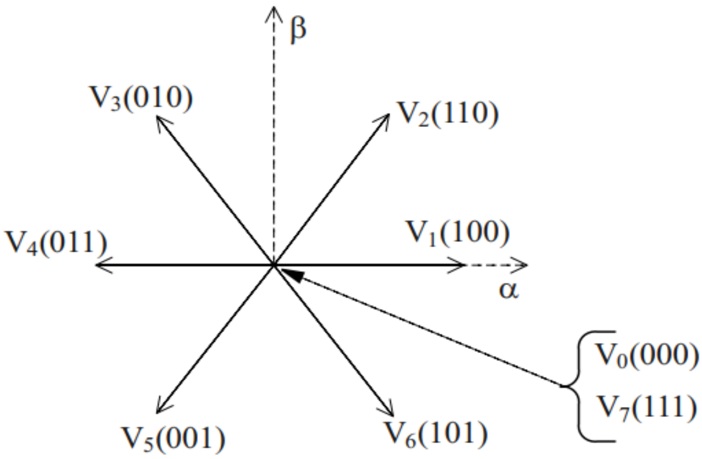

Figure 3.12: Space Vectors Representation of Voltages in αβ-Reference Frame (Abdelhamid & Messaoud, 2021)

The DC bus current i_{dc} can also be represented as

$$i_{dc} = -\begin{pmatrix} i_{ar} & i_{br} & i_{cr} \end{pmatrix} \begin{pmatrix} S_{ar} \\ S_{br} \\ S_{cr} \end{pmatrix} \tag{3.91}$$

Where, i_{ar}, i_{br}, and i_{cr} stands for rotor phase currents in [A].

3.5.2. Grid Side Converter (GSC) Model

This converter is positioned between the DC bus and the power network itself as portrayed in Figure 13. Similar to the MSC, the GSC can work as a rectifier or inverter. It works as a rectifier in hypo-synchronous mode and vice versa. Its main purpose is to sustain the DC bus voltage in a steady state and govern the real and reactive power exchanges between the power network and the converter itself.

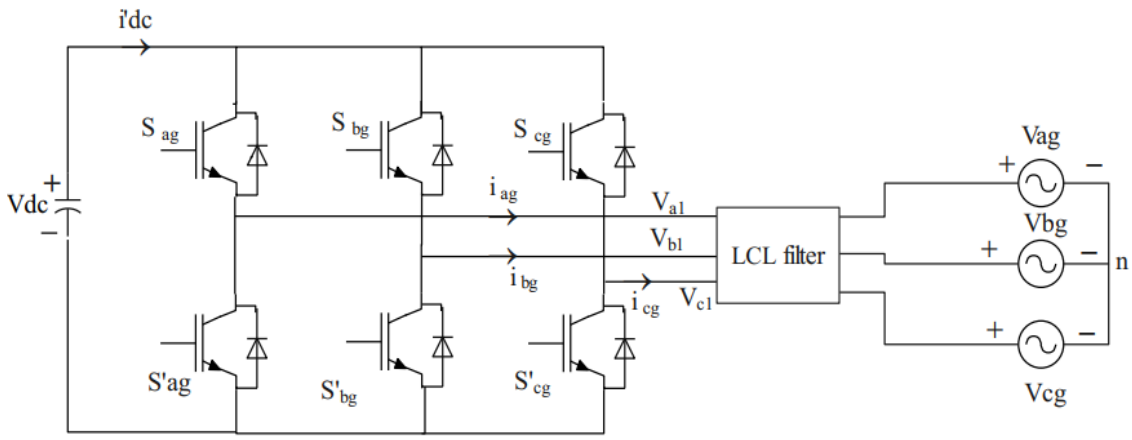

Figure 3.13: Power Circuit of Grid Side Converter (GSC) (Milicua & Abad, 2016)

Like the MSC, the GSC as established in Figure 3.13 is modelled as

$$\begin{pmatrix} V_{a1n} \\ V_{b1n} \\ V_{c1n} \end{pmatrix} = \frac{V_{dc}}{3} \begin{pmatrix} 2 & -1 & -1 \\ -1 & 2 & -1 \\ -1 & -1 & 2 \end{pmatrix} \begin{pmatrix} S_{ag} \\ S_{bg} \\ S_{cg} \end{pmatrix} \quad (3.92)$$

Where, V_{a1n}, V_{b1n}, V_{c1n}, and S_{ag}, S_{bg}, S_{cg} indicates the GSC voltage outputs phase to the neutral point of a load in [V] and the upper IGBT switch positions of the converter itself. Moreover, the current flow to the power network/grid from the DC bus is expressed by

$$i_{dc}^{'} = \begin{pmatrix} i_{ag} & i_{bg} & i_{cg} \end{pmatrix} \begin{pmatrix} S_{ag} \\ S_{bg} \\ S_{cg} \end{pmatrix} \quad (3.93)$$

Where, i_{ag}, i_{bg}, and i_{cg} represents the output GSC phase currents in [A].

3.6. DC Bus Model

This is employed with a capacitor to stabilise the power variations among the rotor and network side converters by keeping the voltage terminal in a steady state and is located in between them as manifested in Figure 3.14.

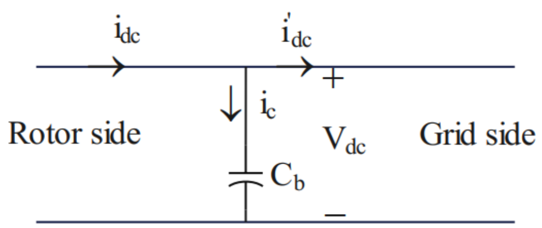

Figure 3.14: DC Bus System (Tuka, 2020)

The DC link voltage in terms of the capacitor current i_c is given by

$$V_{dc} = \frac{1}{C_b} \int i_c dt \tag{3.94}$$

Where, C_b is the DC bus/link capacitance in [F].

The current flow through the capacitance from equation (3.94) is expressed as

$$i_c = C_b \frac{dV_{dc}}{dt} = i_{dc} - i_{dc}^{'} \tag{3.95}$$

Where, $i_{dc}^{'}$ denotes the DC current flow to the power network from the DC bus.

If the converter power losses are neglected, the conservative power relation between the grid AC source and DC bus is expressed by

$$P_g = V_{dc} i_{dc}^{'} \tag{3.96}$$

Where, P_g states the real power transferred to the power network/grid itself with the rotor circuit.

Substituting equation (3.96) into (3.95) results in

$$C_b \frac{dV_{dc}}{dt} = i_{dc} - \frac{P_g}{V_{dc}} \tag{3.97}$$

Equation (3.97) illustrates that the active power can control the DC link voltage.

3.7. Filter Model

To minimize the voltage and current harmonics generated during converter switching, a filter is applied. It is located between the GSC as well as the power network. Based on the numerous features of converters, there are different filter topologies. Considering filtering performance and cost, an LCL filter is contemplated in this study (Kim & Kim, 2016; Park & Burkart, 2018).

Replacing the voltages formed from the PEC as delineated in Figure 3.13 with variable AC voltage sources yields Figure 3.15.

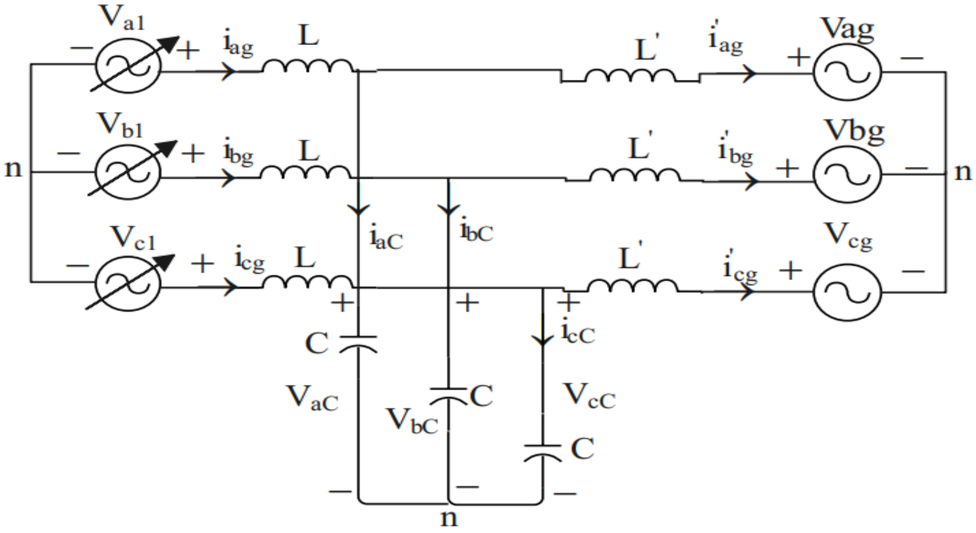

Figure 3.15: LCL Filter (Milicua & Abad, 2016)

Therefore, the electrical equations of the grid-linked converter with an LCL filter are developed from Figure 3.15 by:

$$V_{aC} = -L\frac{di_{ag}}{dt} + V_{a1} \tag{3.98}$$

$$V_{bC} = -L\frac{di_{bg}}{dt} + V_{b1} \tag{3.99}$$

$$V_{cC} = -L\frac{di_{cg}}{dt} + V_{c1} \tag{3.100}$$

$$V_{ag} + L'\frac{di'_{ag}}{dt} = V_{aC} \tag{3.101}$$

$$V_{bg} + L'\frac{di'_{bg}}{dt} = V_{bC} \tag{3.102}$$

$$V_{cg} + L'\frac{di'_{cg}}{dt} = V_{cC} \tag{3.103}$$

In terms of currents, the voltage drops across the filtering capacitors are represented as:

$$V_{aC} = \frac{1}{C}\int i_{aC}dt \tag{3.104}$$

$$V_{bC} = \frac{1}{C}\int i_{bC}dt \tag{3.105}$$

$$V_{cC} = \frac{1}{C}\int i_{cC}dt \tag{3.106}$$

Moreover, the flow currents through the filtering capacitors can be given as:

$$i_{aC} = i_{ag} - i_{ag}^{'} \tag{3.107}$$

$$i_{bC} = i_{bg} - i_{bg}^{'} \tag{3.108}$$

$$i_{cC} = i_{cg} - i_{cg}^{'} \tag{3.109}$$

Where, L, $L^{'}$, and C defines the converter side and grid side inductive filters in [H], as well as the capacitance of the filter in [F] respectively. V_{a1}, V_{b1}, V_{c1}, V_{ag}, V_{bg}, V_{cg}, and $i_{ag}^{'}$, $i_{bg}^{'}$, $i_{cg}^{'}$ symbolises the network side converter output voltages in [V], the power network voltages in [V], and the grid current flows in [A] respectively. Furthermore, V_{aC}, V_{bC}, V_{cC}, and i_{aC}, i_{bC}, i_{cC} embodies the voltages in [V] across, and current flows in [A] through filtering capacitors correspondingly.

3.8. Control of DFIG

The DFIG control is executed by governing the machine as well as network side back-to-back variable frequency converters. The machine-side converter (MSC) controls the reactive and active power of the stator individually. This makes the generator more flexible, which empowers the turbine to gain paramount energy from the wind and support the grid with reactive power. The grid-side /network-side converter, on the other hand, preserves the DC bus voltage stable irrespective of the flow direction and magnitude of rotor power.

3.8.1. Machine Side Converter (MSC) Control

In the early ages, indirect vector control (IVC) was used to attain the objectives of MSC. However, due to its quick dynamic response, simple structure, absence of complicated coordinate transformation, and robustness against machine parameters, direct torque control (DTC) is used nowadays (Sahri et al., 2018). So, in this thesis, DTC is applied to directly control the torque and rotor flux of the machine while controlling the stator's active and reactive powers indirectly (Abad et al., 2011a). DTC works based on the space vector represented in Figure 3.16.

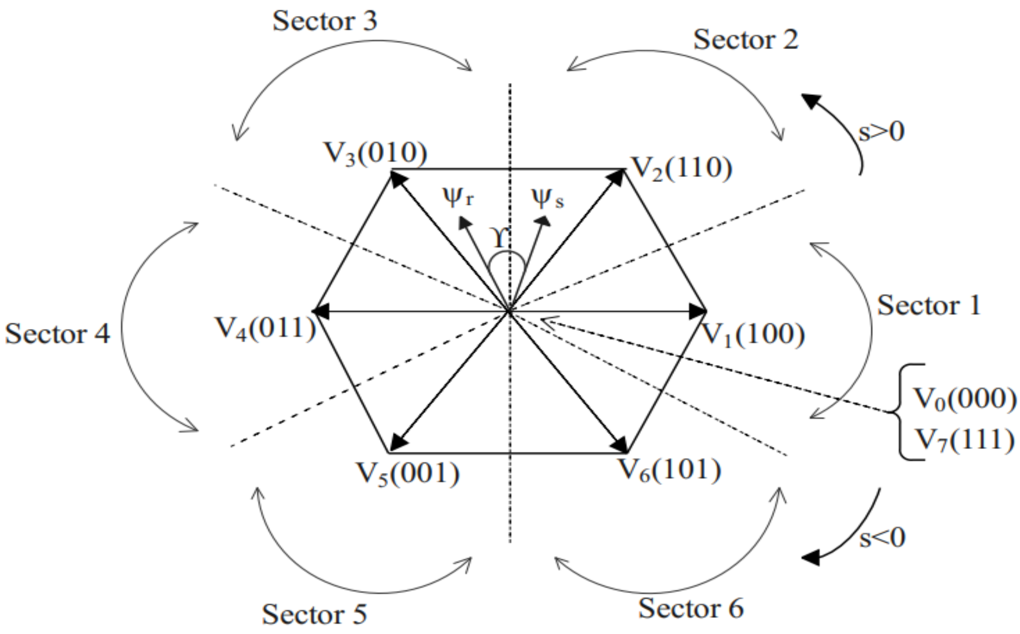

Figure 3.16: Flux Space Vectors in Stationary Reference Frame (Djeriri et al., 2014)

It divides the space vector diagram given in Figure 3.14 into six equal sectors to measure the position of rotor flux. The rotation of stator and rotor side fluxes hinges on the modes of generator operation. Both fluxes revolve in a counterclockwise direction during sub-synchronous mode and vice versa.

The torque delivered in (3.75) can also be re-stated as

$$T_{em} = \frac{3}{2} p \frac{L_m}{mL_s L_r} /\psi_r //\psi_s / \sin\gamma \qquad (3.110)$$

Where, γ symbolises the angle between stator as well as rotor fluxes.

Equation (3.110) implies that the torque relies upon the rotor as well as stator fluxes and the angle between them.

As the direct pairing of the generator stator terminal to the power network, the stator flux space vector has a constant rotating speed and amplitude. Thus, the torque magnitude can be managed by regulating the angle γ and rotor flux amplitude. The rotor flux magnitude is influenced by the voltage vectors added into the rotor of the generator. Moreover, the entire DTC diagram is depicted in Figure 3.17 as follows.

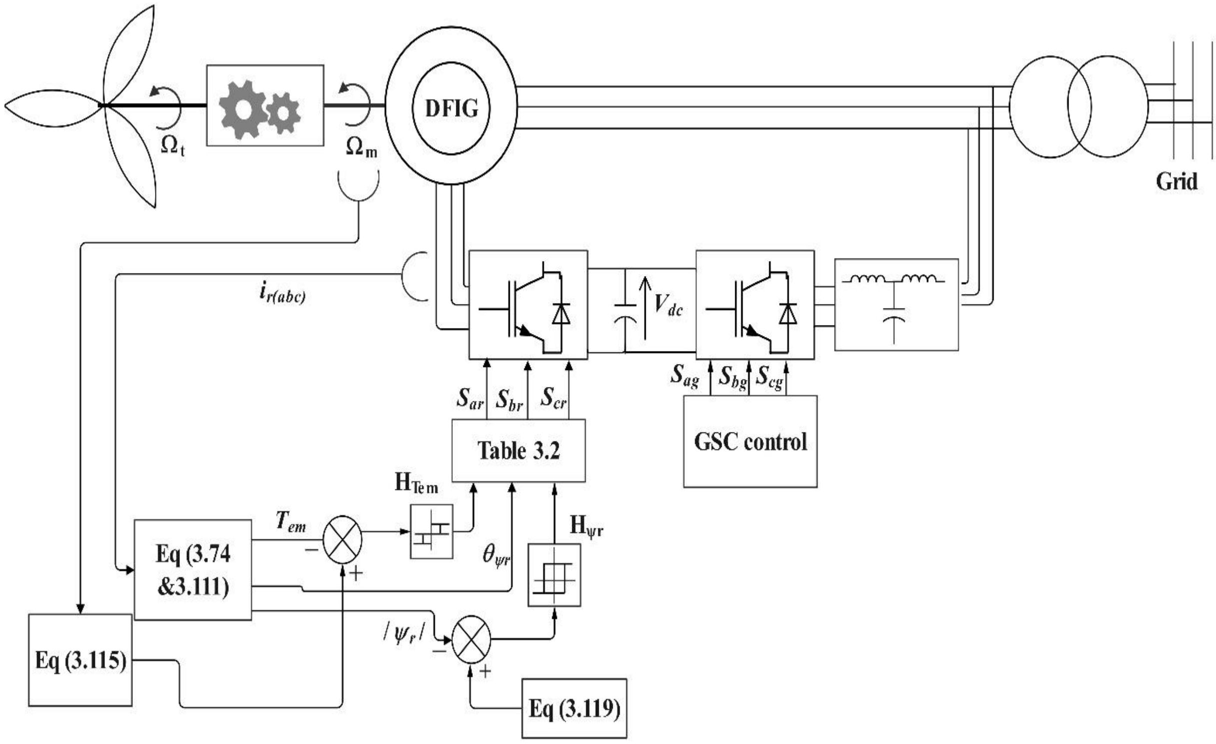

Figure 3.17: DTC Structure of Machine Side Converter

Where, H_{Tem} and $H_{\psi r}$ represents the output hysteresis controls of the electromagnetic torque and flux respectively.

This control structure can be partitioned into the following duties.

- ✓ Rotor flux and torque estimation
- ✓ Generation of torque as well as rotor flux references
- ✓ Voltage vector selection

i) Rotor flux and Torque Estimation

The torque, and rotor flux are determined from quantified magnitudes of the generator. From relations (3.68) and (3.69) , the rotor flux magnitude $/\psi_r/$ in [Wb] is estimated by

$$/\psi_r/ = \sqrt{\psi_{\alpha r}^2 + \psi_{\beta r}^2} \tag{3.111}$$

Moreover, its angle $\theta_{\psi r}$ in degree can be calculated as

$$\theta_{\psi r} = \tan^{-1}(\frac{\psi_{\beta r}}{\psi_{\alpha r}}) \tag{3.112}$$

Similarly, the torque from $\alpha\beta$ - rotor currents and flux is estimated with equation (3.74).

ii) Torque and Rotor Flux Reference Generations

Neglecting the potential drop across the stator resistor, the magnitude of stator flux $/\psi_s/$ from equation (3.34) in terms of stator voltage magnitude $/V_s/$ can be given by

$$/\psi_s/ \simeq \frac{/V_s/}{\omega_s} \tag{3.113}$$

DFIG wind turbine generators operate with constant reactive power references. The three-phase stator reactive power reference Q_s^{ref} using expressions (3.53) and (3.113) can also be stated as

$$Q_s^{ref} = 3\,\mathrm{Im}(V_s I_s^*) = 3\omega_s / I_s / /\psi_s / \cos\varphi \tag{3.114}$$

Where, φ defines the angle between stator flux and current.

Applying equation (3.12) and neglecting the convertor loss, the reference torque T_{em}^{ref} is given by

$$T_{em}^{ref} = \frac{P_{opt}}{\Omega_m} = \frac{1}{2}\rho\pi\frac{R^5}{\lambda_{opt}^3}C_{P\max}\frac{\Omega_m^2}{g^3} \tag{3.115}$$

Similarly, the three-phase torque reference using relation (3.59) may also defined with

$$T_{em}^{ref} = 3p\,\mathrm{Im}(\psi_s^* I_s) = 3p / I_s / /\psi_s / \sin\varphi \tag{3.116}$$

Merging equations (3.113), (3.114) and (3.116) produces

$$I_s = \frac{Q_s^{ref}}{3V_s} + j\frac{T_{em}^{ref}\omega_s}{3pV_s} \tag{3.117}$$

Thus, considering expressions (3.32) and (3.117), the rotor flux reference ψ_r^{ref} can be calculated by

$$\psi_r^{ref} = \left\{\left(\frac{L_r / V_s /}{L_m\omega_s} - \frac{mL_r L_s Q_s^{ref}}{3L_m / V_s /}\right) - j\left(\frac{mL_r L_s \omega_s T_{em}^{ref}}{3pL_m / V_s /}\right)\right\} \tag{3.118}$$

Moreover, its magnitude is shown in equation (3.119) as

$$/\psi_r^{ref}/ = \sqrt{\left(\frac{L_r /V_s/}{L_m \omega_s} - \frac{m L_r L_s Q_s^{ref}}{3L_m /V_s/}\right)^2 + \left(\frac{m L_r L_s \omega_s T_{em}^{ref}}{3pL_m /V_s/}\right)^2} \tag{3.119}$$

iii) Voltage Vector Selection

A conventional DTC scheme picks the demanded voltage vector (optimal switch) from the rotor flux and torque errors to bring them to their hysteresis band values applying the on/off hysteresis controllers as presented in Figure 3.17. The torque controller employs a three-level hysteresis comparator, while the rotor flux controller uses a two-level. Based on the torque error value, its hysteresis controller output may result in a value of -1, 0, or 1. In the same way, the hysteresis output values of the rotor fluxes can merely take a value of -1 or 1 based on their input rotor flux errors.

According to the torque and rotor flux hysteresis controller signal outputs, and space vector position of the rotor flux, the proper voltage to be selected is presented in Table 3.2 below.

Table 3.2: Voltage Vectors Selection (Optimum Switching Table)

Hysteresis controller outputs		Sector number					
H_{Tem}	$H_{\psi r}$	1	2	3	4	5	6
1	1	V_2	V_3	V_4	V_5	V_6	V_1
0		V_7	V_0	V_7	V_0	V_7	V_0
-1		V_6	V_1	V_2	V_3	V_4	V_5
1	-1	V_3	V_4	V_5	V_6	V_1	V_2
0		V_0	V_7	V_0	V_7	V_0	V_7
-1		V_5	V_6	V_1	V_2	V_3	V_4

3.8.2. Grid Side Converter (GSC) Control

This control is responsible for regulating the DC voltage and reactive power flow between the back-to-back converter and the grid itself.

This side converter employs an indirect vector control as it is connected to a quality-proof grid with a fixed frequency, which is a grid voltage-oriented one.

In other words, the power network voltage is aligned to the d-axis synchronous reference frame and diagrammatically it is displayed in Figure 3.18 below.

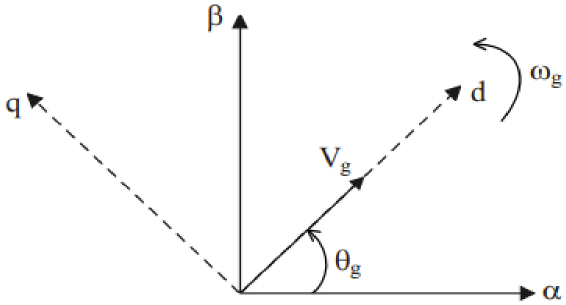

Figure 3.18: Grid Voltage Alignment with d-axis Synchronous Reference Frame (Velpula & Rajaram, 2022)

Where, θ_g and ω_g are the grid voltage angle in degree and angular velocity in [rad/s] respectively.

Mathematically their relation is expressed by

$$\theta_g = \int(\omega_g dt) = \tan^{-1}\left(\frac{V_{\beta g}}{V_{\alpha g}}\right) \tag{3.120}$$

Applying equations (3.98) up to (3.103), the following three expressions will be delivered.

$$V_{a1} = L\frac{di_{ag}}{dt} + L'\frac{di'_{ag}}{dt} + V_{ag} \tag{3.121}$$

$$V_{b1} = L\frac{di_{bg}}{dt} + L'\frac{di'_{bg}}{dt} + V_{bg} \tag{3.122}$$

$$V_{c1} = L\frac{di_{cg}}{dt} + L'\frac{di'_{cg}}{dt} + V_{cg} \tag{3.123}$$

In a stationary $(\alpha\beta)$ reference frame, the calculations given from (3.121) to (3.123) are defined as

$$V_{\alpha 1} = L\frac{di_{\alpha g}}{dt} + L'\frac{di'_{\alpha g}}{dt} + V_{\alpha g} \tag{3.124}$$

$$V_{\beta 1} = L\frac{di_{\beta g}}{dt} + L'\frac{di'_{\beta g}}{dt} + V_{\beta g} \tag{3.125}$$

Similarly, the above two expressions in (dq) reference frame using Park conversion provided in Appendix B can be represented by

$$V_{d1} = L\frac{di_{dg}}{dt} + L^{'}\frac{di_{dg}^{'}}{dt} + V_{dg} - \omega_g L i_{qg} - \omega_g L^{'} i_{qg}^{'} \tag{3.126}$$

$$V_{q1} = L\frac{di_{qg}}{dt} + L^{'}\frac{di_{qg}^{'}}{dt} + V_{qg} + \omega_g L i_{dg} + \omega_g L^{'} i_{dg}^{'} \tag{3.127}$$

The active as well as reactive power flows among the power network and network side converter are shown in equations (3.128) and (3.129) below.

$$P_g = 1.5\,\mathrm{Re}\left\{V_g I_g^{'*}\right\} = 1.5\left(V_{qg} i_{qg}^{'} + V_{dg} i_{dg}^{'}\right) \tag{3.128}$$

$$Q_g = \mathrm{Im}\left\{V_g i_g^{'*}\right\} = 1.5\left(-V_{dg} i_{qg}^{'} + V_{qg} i_{qg}^{'}\right) \tag{3.129}$$

As the d-axis is uniformed with the network voltage, $V_{qg} = 0$. So, the following two expressions will be achieved.

$$P_g = 1.5 i_{dg}^{'} V_{dg} \tag{3.130}$$

$$Q_g = -1.5 i_{qg}^{'} V_{dg} \tag{3.131}$$

Considering $m_1 = V_{dg} - \omega_g L i_{qg} - \omega_g L^{'} i_{qg}^{'}$ and $m_2 = \omega_g L i_{dg} + \omega_g L^{'} i_{dg}^{'}$, equations (3.126) and (3.127) yields

$$V_{d1} = L\frac{di_{dg}}{dt} + L^{'}\frac{di_{dg}^{'}}{dt} + m_1 \tag{3.132}$$

$$V_{q1} = L\frac{di_{qg}}{dt} + L^{'}\frac{di_{qg}^{'}}{dt} + m_2 \tag{3.133}$$

Assuming that the output network/grid side converter and the power network itself current flows are the same (i.e., $i_g = i_g^{'}$), the Laplace transform of the above two equations in their current form gives

$$i_{dg}^{'}(s) = \frac{(V_{d1}(s) - m_1)}{s(L + L^{'})} \tag{3.134}$$

$$i'_{qg}(s) = \frac{(V_{q1}(s) - m_2)}{s(L + L')} \tag{3.135}$$

Taking m_1 and m_2 as a cancellation of coupling terms and considering the converter as well as grid side inductive filters are equal (i.e., $L = L'$), the plant model $P(s)$ for the current loop control is represented by

$$P(s) = \frac{i'_{dg}}{V_{d1}} = \frac{i'_{qg}}{V_{q1}} = \frac{1}{2Ls} \tag{3.136}$$

So, the dq grid current control loops applying a proportional integral (PI) regulator can be shown as

$$V_{d1} = (2Ls)i'_{dg} = (k_{pig} + \frac{k_{iig}}{s})(i'^{ref}_{dg} - i'_{dg}) \tag{3.137}$$

$$V_{q1} = (2Ls)i'_{qg} = (k_{pig} + \frac{k_{iig}}{s})(i'^{ref}_{qg} - i'_{qg}) \tag{3.138}$$

Where, i'^{ref}_{dg}, i'^{ref}_{qg}, k_{pig}, and k_{iig} stands for the reference d -axis as well as q-axis grid currents and parameters of the PI regulator for controlling these grid currents.

Equations (3.137) and (3.138) as a transfer function of the real and reference currents may also be re-stated as

$$\frac{i'_{dg}}{i'^{ref}_{dg}} = \frac{i'_{qg}}{i'^{ref}_{qg}} = \frac{sk_{pig} + k_{iig}}{s^2 + \frac{sk_{pig} + k_{iig}}{2L}} \tag{3.139}$$

Thus, through equalising the denominators of expression (3.139) to a second order denominator of ordinary regulator theories, the parameters of PI controller will be calculated as given below.

$$s^2 + \frac{sk_{pig} + k_{iig}}{2L} = s^2 + 2\xi\omega_n s + \omega_n^2 \tag{3.140}$$

Considering $\xi = 1$, k_{pig} and k_{iig} will be evaluated as

$$k_{pig} = 4\omega_n L \tag{3.141}$$

$$k_{iig} = 2\omega_n^2 L \tag{3.142}$$

In the same manner, the parameters of PI regulator for controlling the DC bus voltage are derived as follows.

From equation (3.95), the transfer function of DC bus voltage to be regulated is represented by

$$C_b s V_{dc} = (k_{pVdc} + \frac{K_{iVdc}}{s})(V_{dc}^{ref} - V_{dc}) \quad (3.143)$$

$$\frac{V_{dc}}{V_{dc}^{ref}} = \frac{sk_{pVdc} + k_{iVdc}}{C_b s^2 + sk_{pVdc} + k_{iVdc})} \quad (3.144)$$

Where, V_{dc}^{ref} , k_{pVdc}, and K_{iVdc} indicates the reference DC bus voltage and its PI controlling parameters respectively.

So, equating the denominators of expression (3.144) to a second-order denominator of ordinary control theories, k_{pVdc}, and K_{iVdc} will be expressed as

$$k_{pVdc} = 2\omega_n C_b \quad (3.145)$$

$$K_{iVdc} = \omega_n^2 C_b \quad (3.146)$$

Considering unity power factor operation (i.e., $Q_g = 0$), the complete structure of GSC is portrayed in Figure 3.19.

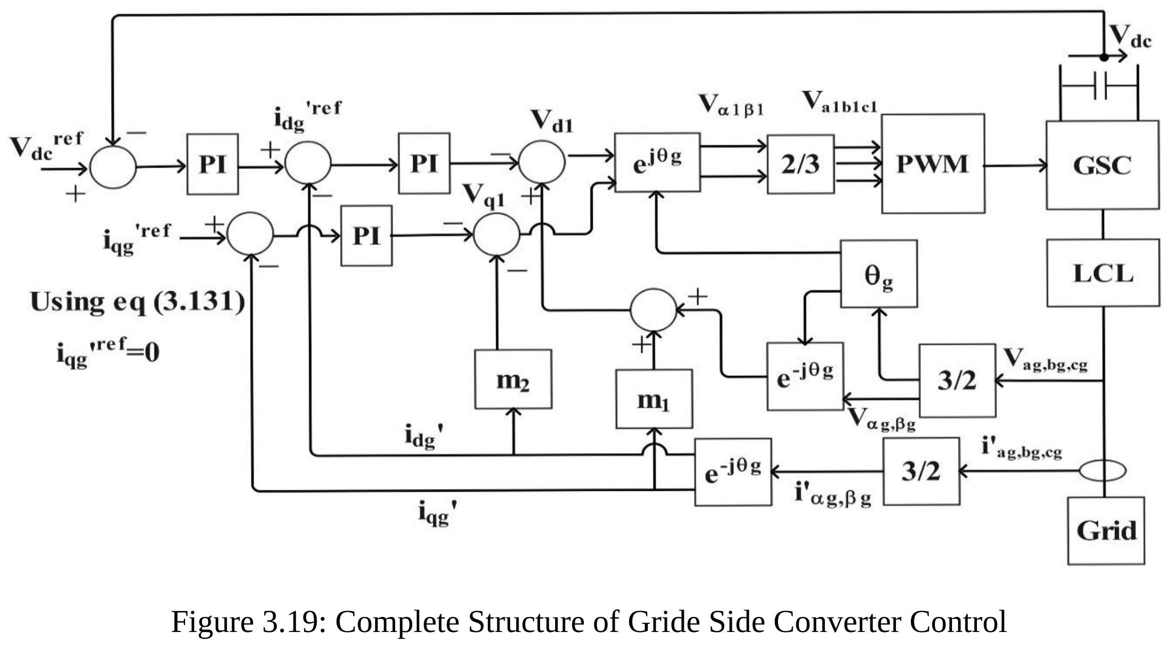

Figure 3.19: Complete Structure of Gride Side Converter Control

3.9. Series Dynamic Braking Resistor (SDBR) Modelling

Modelling of this resistor is necessary to determine its proper value as lower magnitude of the resistor is incapable of limiting fault current and high-value encounters large dissipation energy (Karkri et al., 2018).It value should be minimum to limit the generator stator voltage from surpassing its upper value so that equation (3.147) is satisfied.

$$V_g + V_{SDBR} \leq V_{s\lim} \tag{3.147}$$

Where, V_g, V_{SDBR}, and $V_{s\lim}$ stands for grid, SDBR, and maximum stator voltages in [V] correspondingly.

This dynamic resistor also needs to be sufficient enough to restrict the rotor voltage during the fault to the upper voltage magnitude of the machine-side converter to minimise damage on the back-to-back converter.

$$V_{r\lim} \leq V_{MSC\lim} \tag{3.148}$$

Where, $V_{r\lim}$, and $V_{MSC\lim}$ represents the maximum voltages of the rotor itself in the fault period and machine side converter respectively.

In normal operation, the MSC should induce a voltage less than the DC bus bar voltage and it is declared by

$$V_{MSC\lim} = \frac{V_{dc}}{2\sqrt{\frac{2}{3}}} \tag{3.149}$$

Considering the worst voltage dip case $V_g = 0$ and replacing V_{SDBR} by $R_{SDBR} I_s$, equations (3.147)-(3.149) can be re-written as

$$\left\{ V_s - \frac{V_{dc}}{2\sqrt{\frac{2}{3}}} \right\} \left(\frac{1}{I_s} \right) \leq R_{SDBR} \leq \frac{V_{s\lim}}{I_s} \tag{3.150}$$

Where, R_{SDBR} stands for the value of SDBR in [Ω]. So, substituting the parameter values of equation (3.150) yields

$$0.03\Omega \leq R_{SDBR} \leq 0.68\Omega \tag{3.151}$$

CHAPTER 4

RESULTS AND DISCUSSIONS

4.1. Introduction

Applying MATLAB/Simulink 2021a software, a comprehensive analysis is carried out in this chapter to evaluate the DFIG wind turbine's performance in normal and abnormal circumstances. In abnormal conditions, a fuzzy logic-controlled crowbar and a hybrid crowbar with SDBR protection-based schemes are adopted to analyse the LVRT-enhancing capability of this wind turbine. The primary data/parameters applied to model this generator are indexed in Appendix A.1.

4.2. Simulink Model Explanation

In this portion, the Simulink model of a DFIG wind power is presented. Figure 4.1 in general contains the DFIG, wind turbine, back-to-back converter, DC link, crowbar, SDBR, and LCL filter. A 1.5 MW rated power of DFIG, which is collected from Adama-II wind power, is used in this model considering its variable wind speed operation and smaller converter costs. Its stator winding is directly linked to a 50 Hz national grid while its rotor is coupled to the power network via a back-to-back PEC namely grid side (GSC) and machine side converters (MSC). A DTC is used in MSC to maintain the rotor flux and torque directly and stator reactive power indirectly, however, an indirect vector control (IVC) is applied in GSC to regulate the DC bus voltage. Moreover, a fuzzy logic-controlled crowbar and SDBR are combined in this model to enhance the LVRT capacity of the generator in transitory moments.

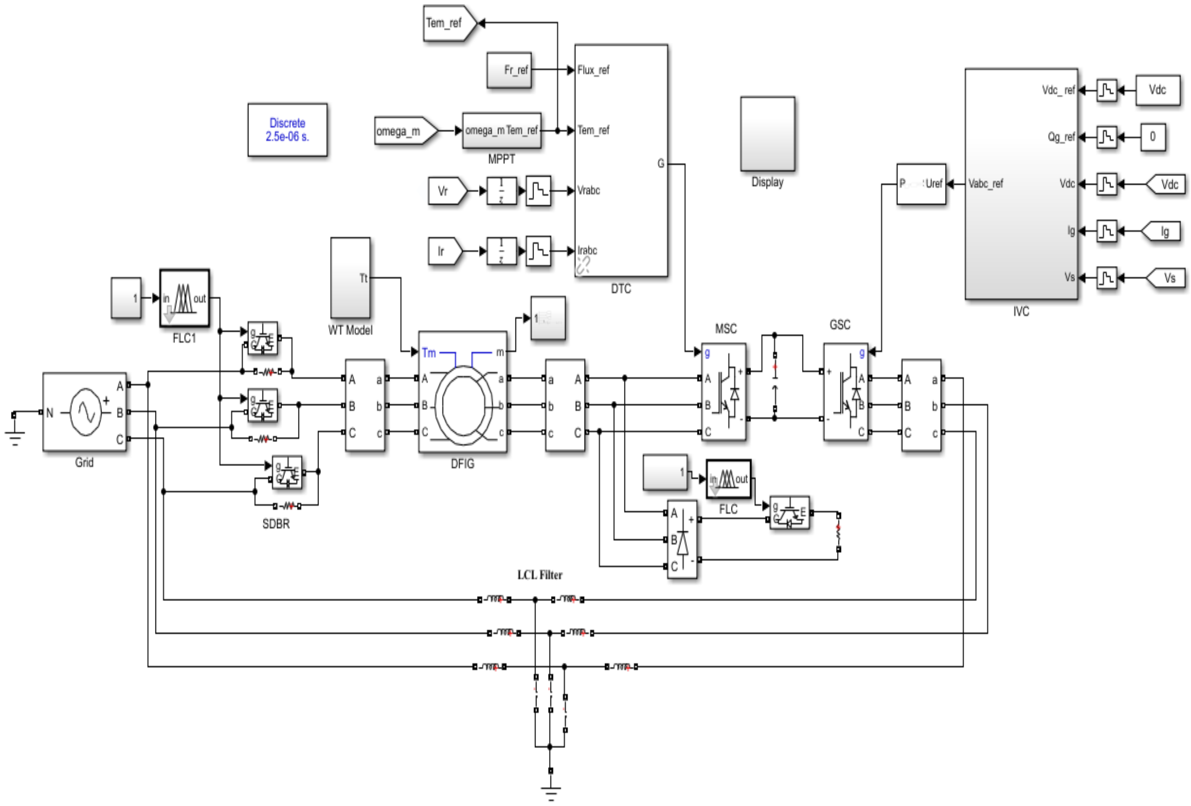

Figure 4.1: Overall Simulink Model of DFIG WTGS

4.2.1. Machine Side Converter Control Model

Figure 4.2 represents the Simulink model of MSC control. This model is performed with the help of reference frame theory by transforming the three-phase components into a stationary two-phase reference frame using Clarke transformation as defined in Appendix B. As stated before, the MSC is in charge of regulating the rotor flux and torque. The torque and rotor flux magnitudes are estimated from the two-phase stationary reference frames. Then, these measured values are compared to their reference values by the hysteresis torque and rotor flux band controllers. The torque reference is acquired from the maximum power tracking approach while the rotor flux is attained from the reactive power as well as torque references as shown in equation (3.119). After that, an appropriate rotor voltage vector is picked from the optimum switching table depending on hysteresis regulators to maintain the rotor flux and torque magnitudes with their permissible bands. The hysteresis band ranges applied in this thesis are 1% and 3% of their nominal values for the torque and rotor flux respectively.

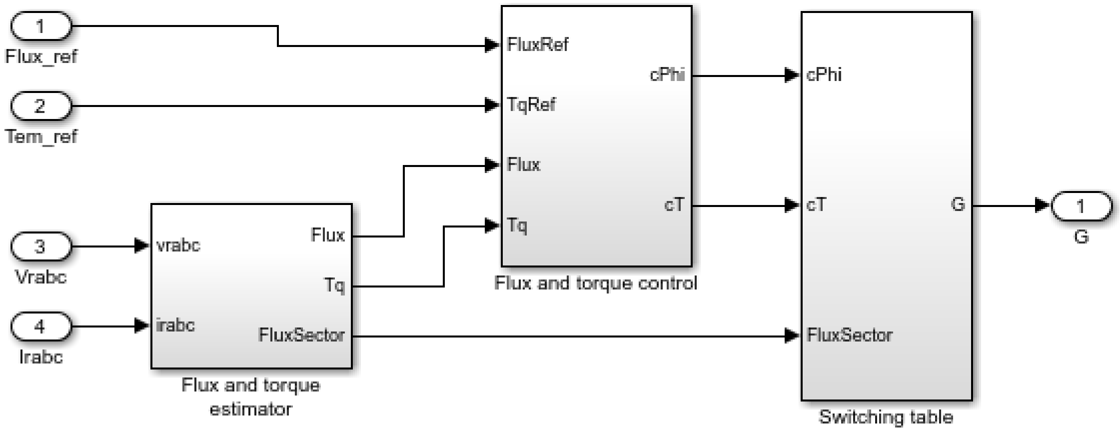

Figure 4.2: Simulink Model of MSC Control

4.2.2. Simulink Model of Grid Side Converter Control

Regulating the DC bus voltage is the primary mandate of GSC. As this converter control model employs IVC, its control begins by comparing the reference and actual values of the DC bus voltage so that the error is fed to the PI regulator. Then, the error in the steady state is eliminated with the PI controller to generate the active power values and d-axis grid current references. To ensure a unity power factor operation of the generator, the value of the grid reactive power reference is appropriated as zero. In the same manner as the MSC, Clarke and Park transformation (which converts a stationary two-phase reference frame into a two-phase rotating reference frame) are employed in this converter control. The actual d and q-axis of the grid/power network currents are obtained by employing the park transformation and compared with their reference values to give the d-axis and q-axis reference voltages by the PI regulator. Finally, the converter output voltage is acquired using inverse Park and Clarke transformations, DC link voltage, and GSC's switching signals.

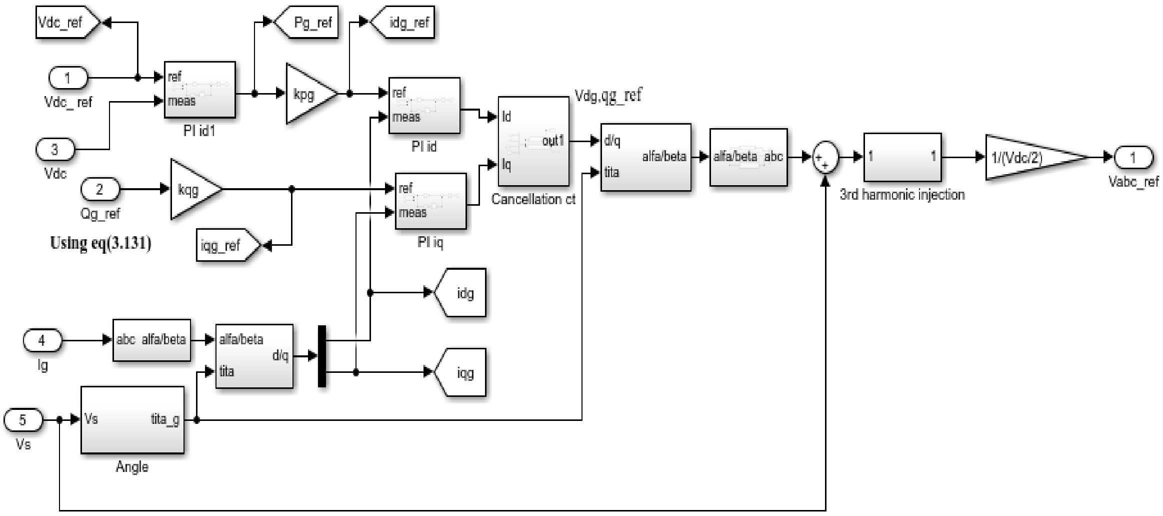

Figure 4.3: Simulink Model of GSC Control

4.2.3. Fuzzy Logic Controlled Crowbar and SDBR Model

In Figure 4.4, the fuzzy logic-controlled crowbar and series dynamic braking resistor is illustrated.

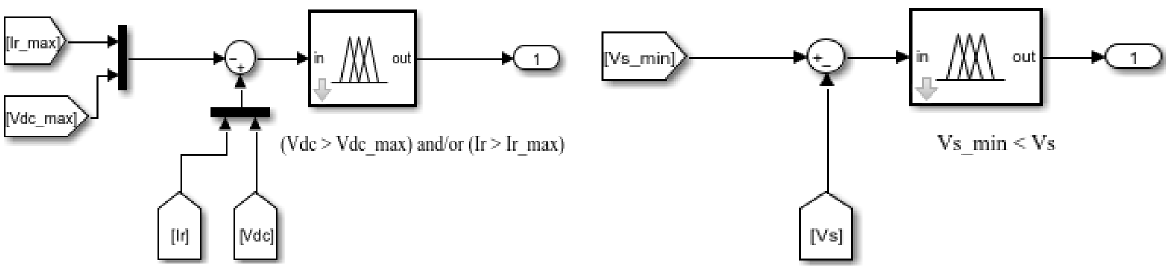

(a) Fuzzy Logic Controlled Crowbar (b) Fuzzy Logic Controlled SDBR

Figure 4.4: FLC Crowbar and SDBR

In the regular operation, the crowbar IGBT switch is in off position, however, the parallel connected IGBT switch of SDBR is turned on and vice versa in transient conditions.

A Sugeno fuzzy inference system is applied to perform the on/off control in both cases as it allows a constant membership function (i.e., 1 and 0 in this case). It gives an output value of 1 to the crowbar IGBT if the actual DC bus voltage and or the rotor current exceeds their maximum value. Similarly, it turns off the parallelly connected IGBT switch with the SDBR if the measured stator voltage drops below its minimum permissible value. In this thesis, the value of SDBR is taken 0.05 ohm considering the derived relations in equation (3.151). Moreover, a triangular membership function is taken in the input side considering its simplicity.

4.3. Simulation Results

4.3.1. DFIG Behaviour During Normal Condition

In normal working condition, the MSC with DTC is in charge of maintaining the rotor flux and torque directly. It also controls the machine speed, and reactive as well as active power transfers indirectly. Maintaining the DC bus voltage at steady state to transmit the demanded power to the grid is the GSC's responsibility and utilizes an IVC as stated before. Moreover, the simulation outcomes of the DFIG WTGS under normal conditions graphically are given in Figures 4.5, 4.6, and 4.7 below.

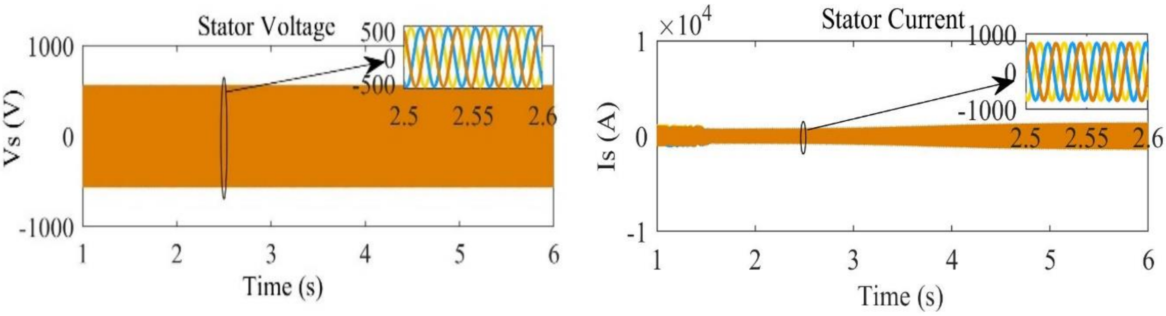

(a) Stator Voltage (b) Stator Current

Figure 4.5: Stator Voltage and Current

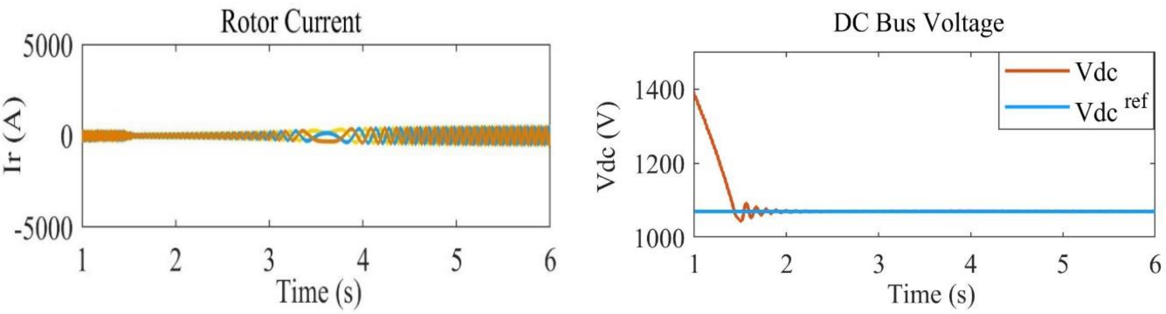

(a) Rotor Current (b) DC Bus Voltage

Figure 4.6: Rotor Current and DC Bus Voltage

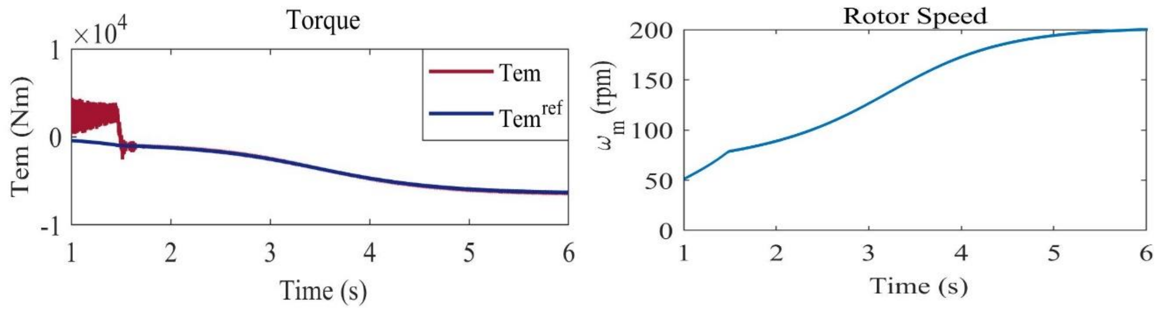

(a) Torque (b) Rotor Speed

Figure 4.7: Torque and Rotor Speed

The stator voltage and currents in steady-state operations are delineated in Figure 4.5 (a) and (b) subsequently. Their result indicates that in normal operation, they are balanced and similar to their nominal values. Figure 4.6 (a) exhibits the stable rotor current value. Even though the rotor current variation happened after the third second due to the initial rotating of the generator with zero rotor speed and 10 m/s normal operation, it is damped around 4 seconds by the control system. As depicted in Figure 4.6 (b), the actual value of the DC bus voltage follows its reference value of 1070V before 2 seconds although there is a variation initially. Similarly, the real value of electromagnetic torque is chasing its reference as illustrated in Figure 4.7 (a). The negative value implies that the machine is working as a generator and a negative torque is applied as input to the wind power Simulink model to use motor input convention so that the system performs as a generator. The rotor speed in a steady state condition is given in Figure 4.7 (b) and is also normal.

4.3.2. DFIG Behaviour During Symmetrical Voltage Dips

Both symmetrical and asymmetrical voltage dips at a PCC affect the performance of DFIG. The consequences of asymmetrical grid faults can be maintained without any hardware protection scheme since the zero sequence components can be relinquished by the D-Y/Y-D transformer connections and controlling the negative sequence components with the DFIG control itself (Endale & Tuka, 2021; Thomas & Prince, 2020). However, even though the symmetrical fault incident is rare, it is so severe that the generator control cannot withstand it. When this fault happens on the power network, the generator stator voltage diminishes which results in stator flux reduction, and the generator will be demagnetised. This further aggravate to the flow of high stator and rotor currents, DC bus voltage expansion, and torque disturbance. As a result, damage to the stator, and back-to-back converter components may happen.

So, this project is solely intended to examine the effects of symmetrical voltage drops on the DFIG's performance and how implementing hardware protection with appropriate control enhances its LVRT capability.

4.3.2.1. DFIG Behaviour During Symmetrical Voltage Dips with Traditional Crowbar

A three-phase 90% symmetrical voltage dip at the point of interconnection (POI) at 2.5 seconds was applied for 150 milliseconds duration to test the DFIG's performance with a conventional crowbar protecting system. So, the simulation results of the balanced fault effect on the machine are presented in Figure 4.8.

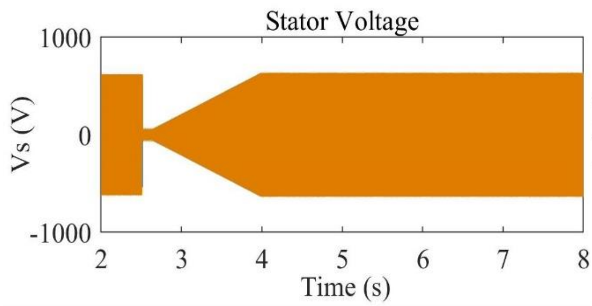

(a) Stator Voltage

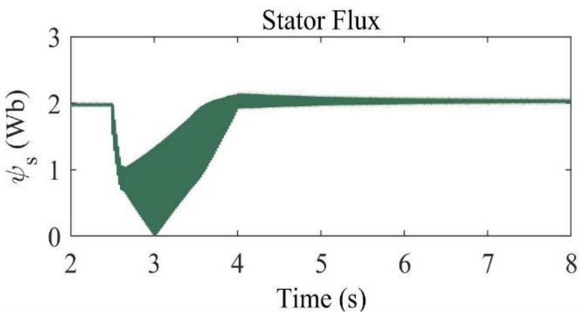

(b) Stator Flux

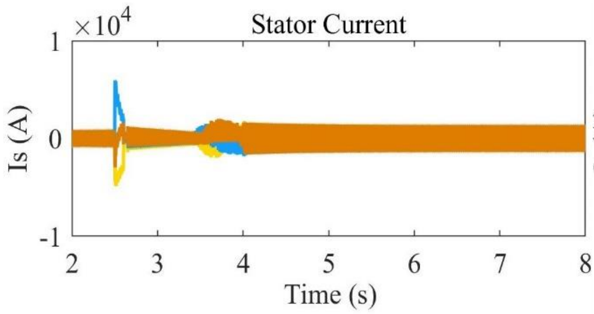

(c) Stator Current

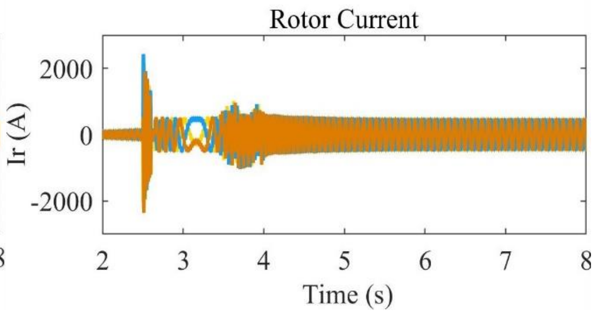

(d) Rotor Current

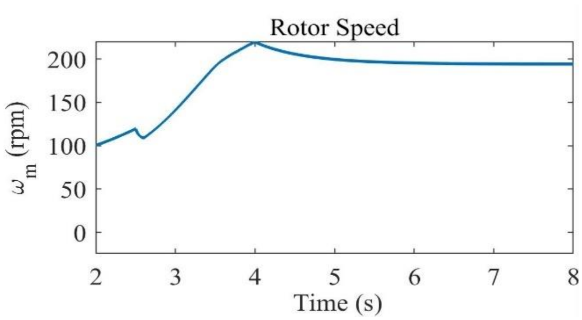

(e) Rotor Speed

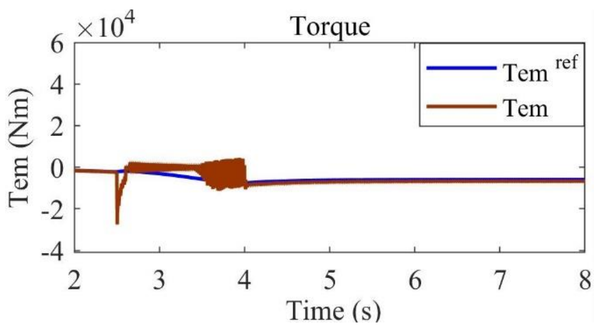

(f) Torque

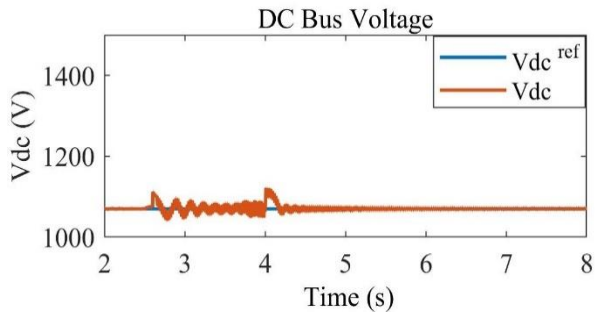

(g) DC Bus Voltage

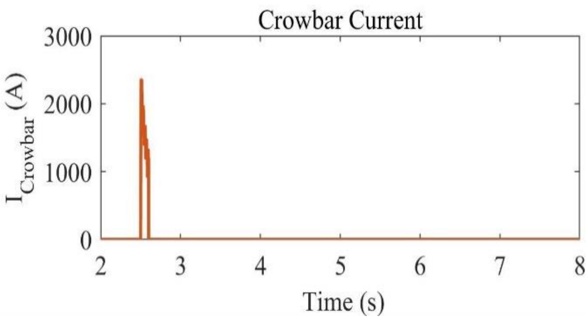

(h) Crowbar Current

Figure 4.8: DFIG Response with Traditional Crowbar Protection

The symmetrical voltage dip causes the generator stator voltage to decrease to its 10% value and decline in its stator flux near to zero as shown in Figure 4.8 (a, b). However, these values are restored to their nominal pre-fault ones at 4 seconds with the help of the traditional crowbar method. The crowbar is integrated into the generator rotor terminal for 100 milliseconds following detection of the voltage dip. Figure 4.8 (c, d) depicts how the inrush stator, as well as rotor currents, are produced due to the fault happening and circulate through the crowbar itself. The speed of the rotor and torque are affected by the grid voltage sag, as exhibited in Figure 4.8 (e, f). Even though the fault was cleared after 150 milliseconds, the torque did not follow its reference value quickly since the torque control was lost during crowbar activation. Figure 4.8 (g, h) indicates the DC bus voltage and crowbar resistance current values. The DC voltage somehow follows its reference value, which is 1070 V after the fault happens. The power converters are protected against the inrush current by damping the fault current displayed in Figure 4.8 (h). After the rotor current is decreased, the crowbar is disabled, and the stator flux regains its former value.

4.3.2.2. DFIG Behaviour During Symmetrical Voltage Dips with FLC Crowbar

Even though the classical crowbar is commonly used for protecting the back-to-back converter from rotor over currents and DC bus over voltages, its activation time prolongs the voltage dip recovery and torque control loss as the converter control is deactivated in its operation. So, FLC is added to improve the crowbar timing through controlling the crowbar IGBT switch. The FLC block turns on/off the switch by comparing the instrumented values of the rotor current and DC bus voltages with their maximum limit values as shown in Appendix A.1. It turns on when both/one of the measured values exceeds their limits.

Thus, the DFIG's performance with FLC crowbar under 90% terminal voltage drop at 2.5 seconds for 150 milliseconds is demonstrated in Figure 4.9.

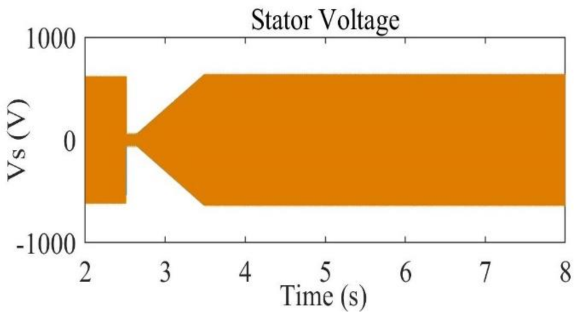

(a) Stator Voltage

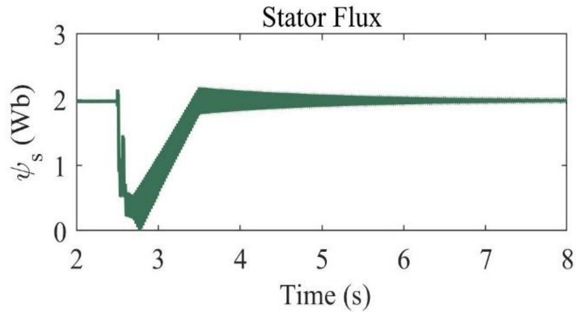

(b) Stator Flux

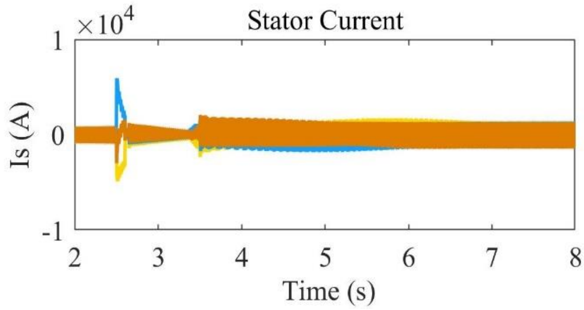

(c) Stator Current

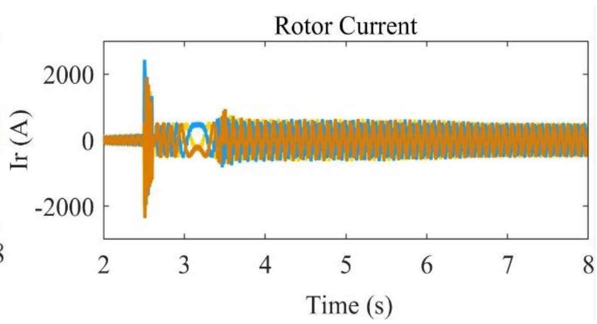

(d) Rotor Current

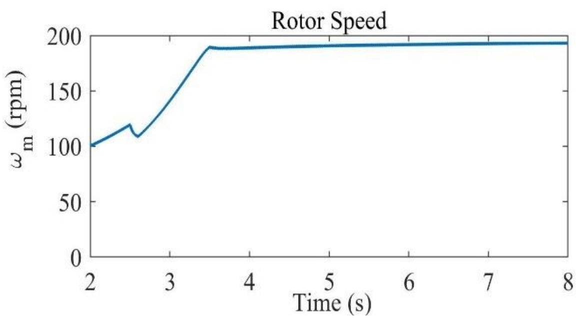

(e) Rotor Speed

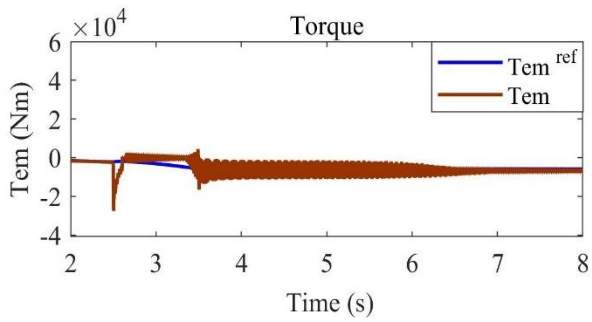

(f) Torque

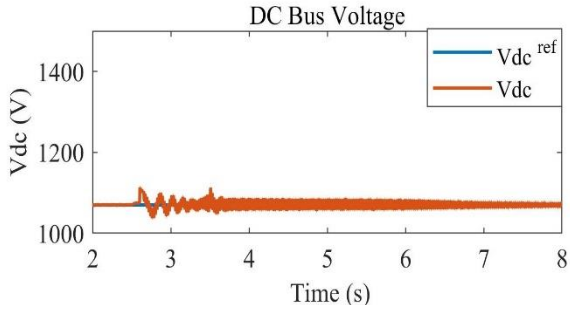

(g) DC Bus Voltage

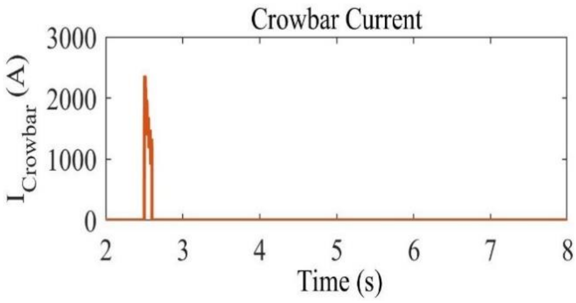

(h) Crowbar Current

Figure 4.9: DFIG Response with FLC Crowbar Protection

As sketched in Figure 4.8 (a, b), the time duration for stator voltage and flux return to their pre-fault values following the symmetrical voltage dip is longer than the values represented in Figure 4.9 (a, b). This has happened since the traditional crowbar activation elongated the terminal voltage recovery. In other words, the FLC block fastens the working time of the crowbar so that the stator voltage and flux recover from the applied dip slightly faster than the conventional crowbar ones. Although the transient magnitudes of the rotor as well as stator currents during the initial connection of both traditional and FLC crowbars look similar, the value shown in Figure 4.9 (c, d) achieves its nominal value following the dip marginally quicker than the former given in Figure 4.8 (c, d). As pictured in Figure 4.8 (e, f), when the crowbar is connected, the speed and torque lose control as the operation of the crowbar inhibits the converter control. For some time, the speed is reduced from its suggested value and the torque seems zero. However, as illustrated in Figure 4.9 (e, f), adding FLC to the crowbar helps the rotor speed return to its nominal value and the torque follows its reference relatively faster than the previous ones. As portrayed in Figure 4.9 (g), the DC voltage varies slightly in the initial connection of the crowbar, however, it regains its pre-fault value following the clearance of the fault.

4.3.2.3. DFIG Behaviour During Symmetrical Voltage Dips with Hybrid FLC Crowbar and SDBR

Although the FLC crowbar improves the recovery time of DFIG, the stator as well as rotor current transients during the initial activation of the crowbar are still high and should be minimised to protect against the failure of DFIG equipment as briefed in the problem of statement including the crowbar itself. So, adding SDBR to the previous FLC crowbar is essential to damp the flow of inrush stator and rotor currents at the very beginning of the crowbar connection so that the damages on the crowbar and generator stator as well as rotor circuits will be reduced while increasing the timing of torque control after the severe dip. Thus, applying the same dip magnitude and its duration with the above two situations, combining fuzzy-controlled SDBR in series with the stator winding enhances the generator's performance as portrayed in Figure 4.10. The FLC block in the SDBR turns on/off its parallelly connected IGBT switch by comparing the measured stator voltage with its minimum permissible value. It turns off when the measured value is below the minimum set voltage, which is 90% of its rated value.

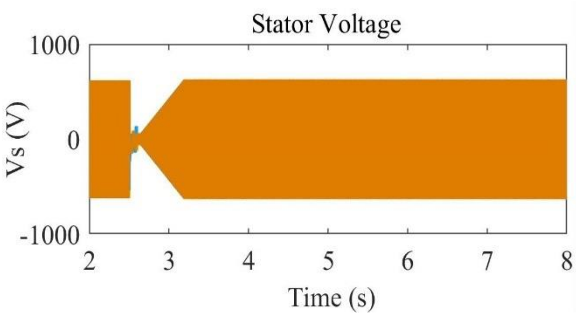

(a) Stator Voltage

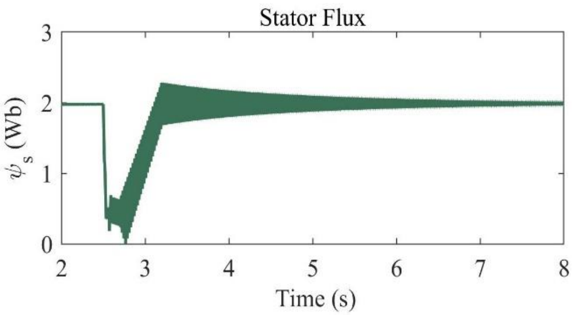

(b) Stator Flux

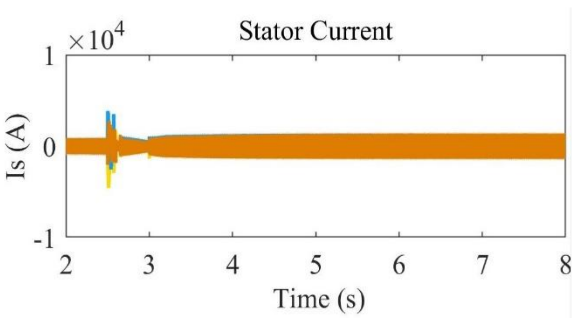

(c) Stator Current

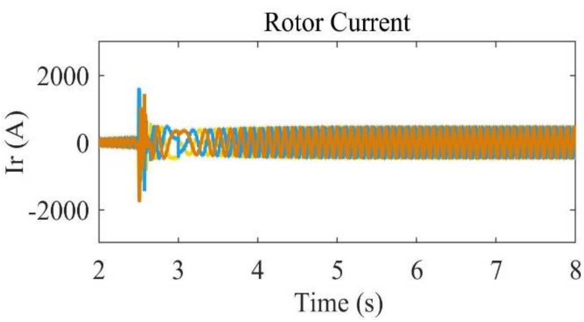

(d) Rotor Current

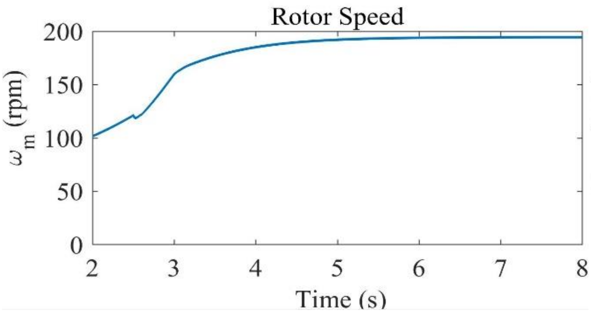

(e) Rotor Speed

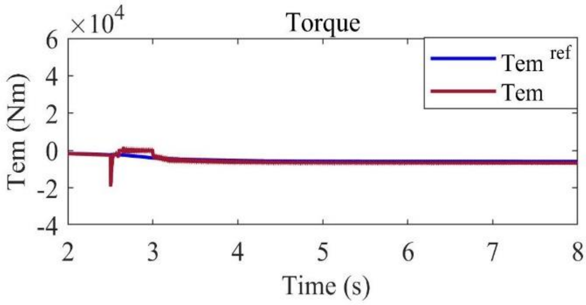

(f) Torque

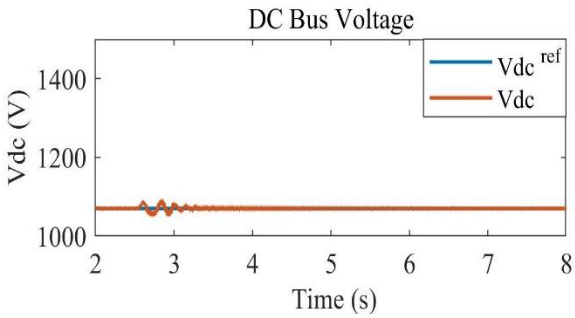

(g) DC Bus Voltage

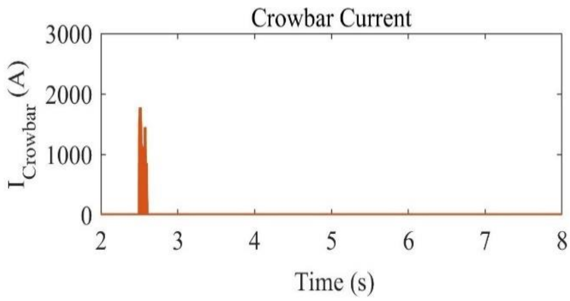

(h) Crowbar Current

Figure 4.10: DFIG Response with Hybrid FLC Crowbar and SDBR

Figure 4.10 (a, b) indicates that the voltage across the generator stator and flux during the pre-fault period were at steady state. However, their magnitudes dropped significantly during the symmetrical dip. Then, they returned to their nominal value with improved timing due to additional SDBR. The stator together with the rotor fault currents created due to the fault incident circulate through the crowbar, as displayed in Figure 4.10 (c, d, h), are to some extent minimised since the braking resistor is joined in series amid the grid voltage sag. As revealed in Figure 4.10 (e, f), the rotor speed of the turbine and torque regained their pre-fault values after the fault was cleared as quickly as possible. This maintains the mechanical stability of the turbine. The effects of DC terminal voltage and current flow through the crowbar resistance during and after the fault incident are illustrated in Figure 4.10 (g, h).

4.4. Comparison of the Results

A meaningful comparison among the parameters of the machine, while facing the symmetrical dip using the traditional crowbar, FLC crowbar, and hybrid FLC crowbar with SDBR schemes is given in Figure 4.11 as follows.

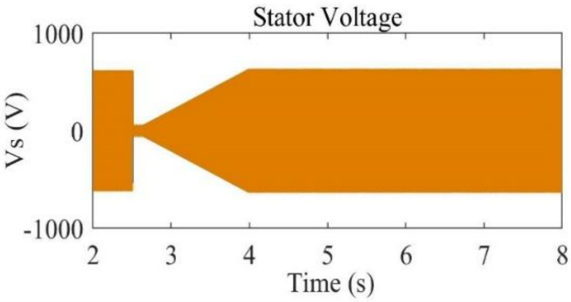

(a1)

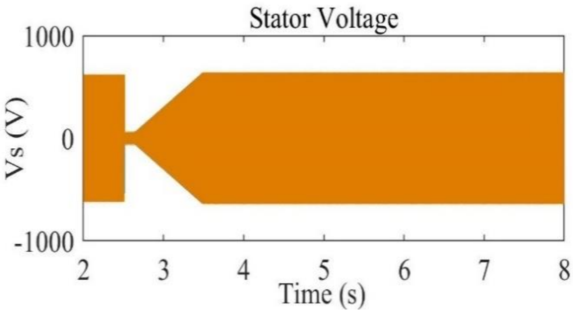

(a2)

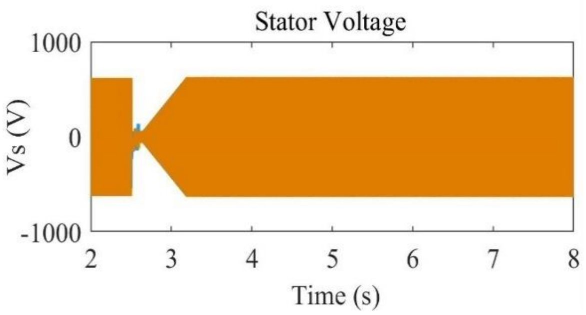

(a3)

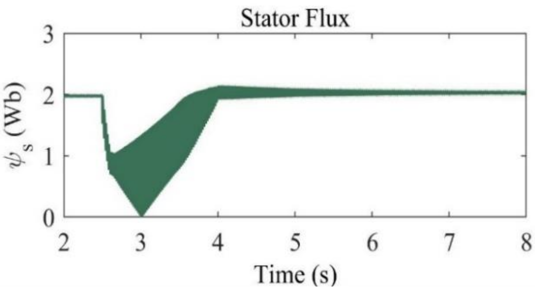

(b1)

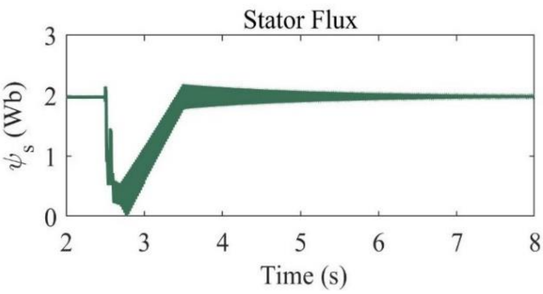

(b2)

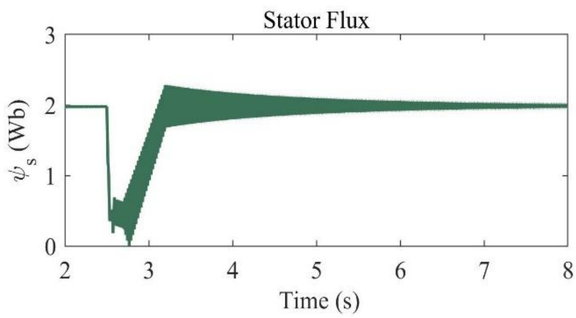

(b3)

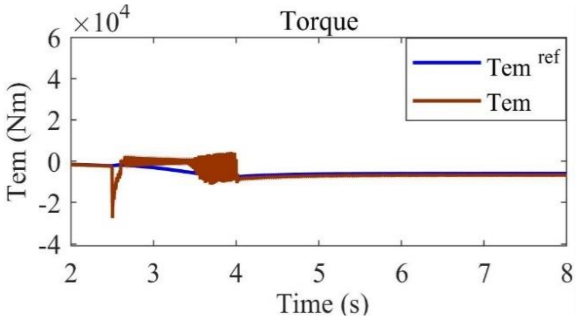

(c1)

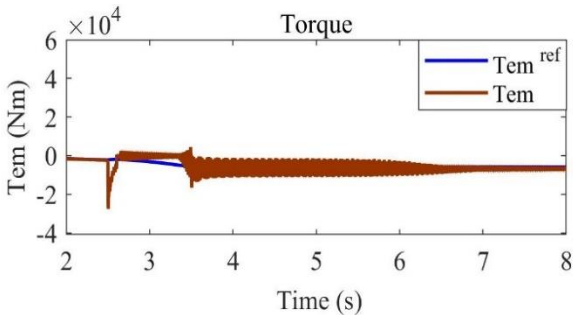

(c2)

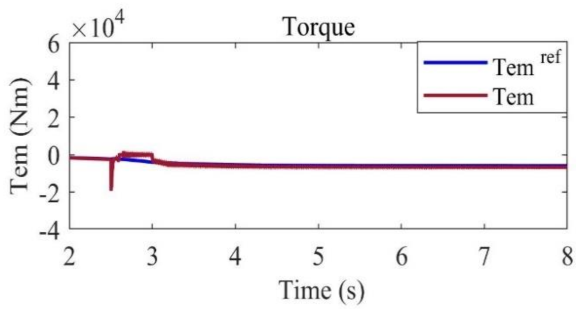

(c3)

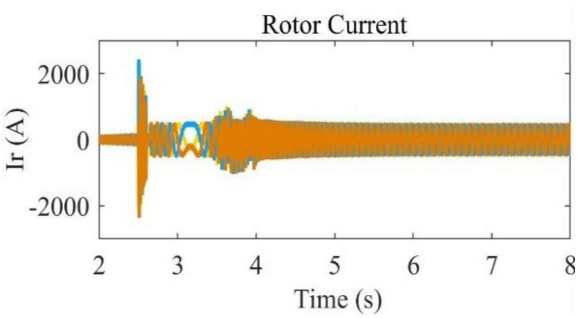

(d1)

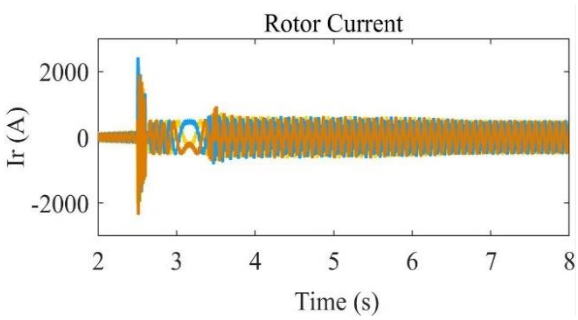

(d2)

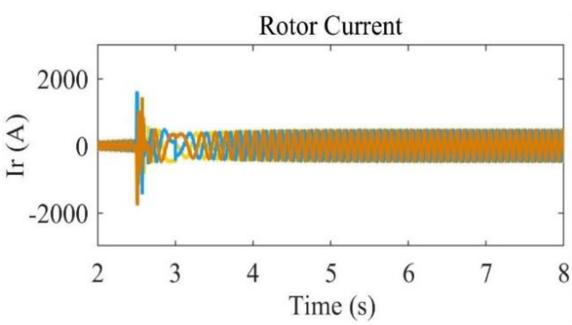

(d3)

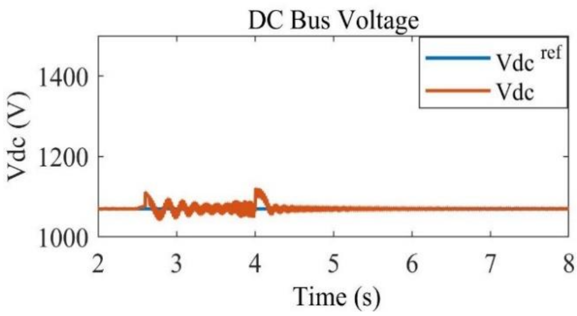

(e1)

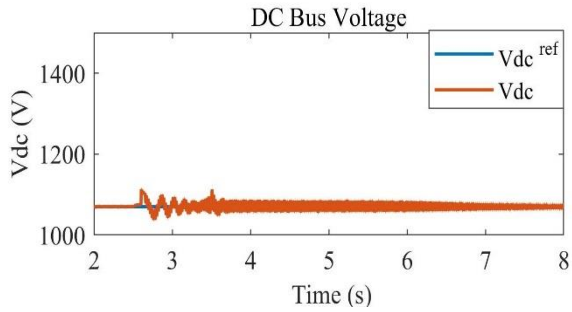

(e2)

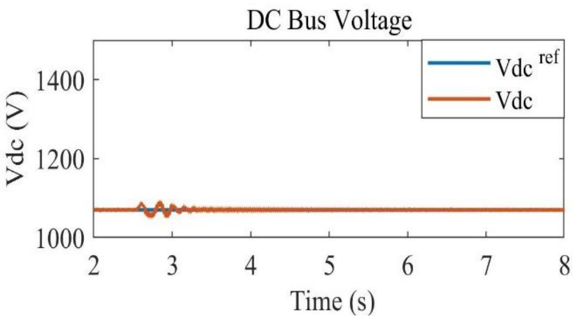

(e3)

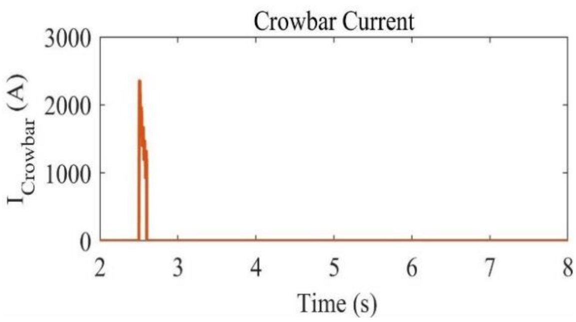

(f1)

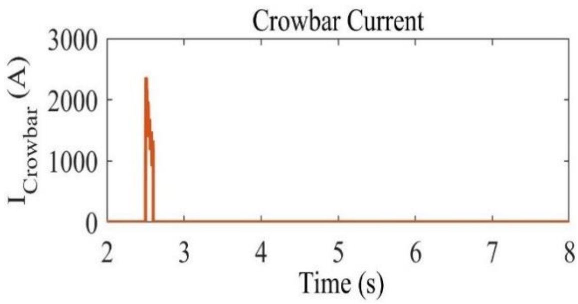

(f2)

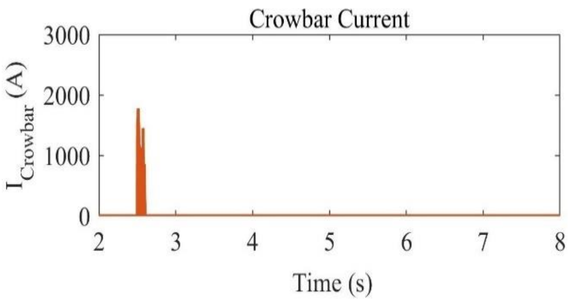

(f3)

Figure 4.11: Comparative Performance Analysis of DFIG

Figure 4.11 emphasizes the comparative performances of the machine parameters. A specific number is provided for each parameter. The parameters with the conventional crowbar, FLC crowbar, and FLC combined crowbar with SDBR are assigned by ‘1’, ‘2’, and ‘3’ respectively. Figure 4.11 (a1, a2, and a3) indicates that the stator voltage decreases substantially during the fault using the classical crowbar, FLC crowbar, and FLC crowbar with SDBR correspondingly. Then, the system with hybrid FLC crowbar and SDBR recovers to its rated value faster than the other two enhancing methods. Similarly, as presented in Figure 4.11 (b1, b2, and b3), the stator flux regains its nominal value quickly with the hybrid one.

The flow of transient rotor currents presented in Figure 11 (c1, c2, and c3) are restored to their pre fault values with the help of the crowbar circuit in all three cases. However, the later enhancing technique increased its recovery time rapidly while minimising its magnitude during the initial activation of the crowbar compared to the other two previous methods. Subfigures (d1 and d2) clarify that the torque control is lost for 1.5 and 1 second with the classical and FLC crowbar ones respectively. However, the machine control loss is reduced to 0.5 seconds by adding the FLC crowbar with SDBR. The measured DC link voltage, as illustrated in subfigures (e1, e2, and e3), in all cases is maintained during the fault period. Nevertheless, its disturbance is low and recovered in a short duration with FLC hybrid crowbar and SDBR. The fault current flow through the crowbar resistor of the three cases is depicted in subfigures (f1, f2, and f3). It implies that the damage on the crowbar component itself during the severe dip in the third case is relatively less compared to the first two.

Moreover, the comparative analysis of these three enhancing schemes under the specified symmetrical dip numerically is elaborated in Table 4.1.

Table 4.1: DFIG Parameter Performance Comparative Analysis

Parameters	Conventional crowbar	FLC crowbar	FLC hybrid crowbar with SDBR
Stator voltage	It returns to its nominal value after 4 seconds.	It regains its rated value at 3.48 seconds.	It recovers to the pre fault value at 3.2 seconds.
Stator flux	It attains its normal magnitude at 3.98 seconds.	It tries to stabilise at 3.51 seconds.	It preserves to nominal value at 3.22 seconds
Rotor current	It inrushes to 2400A and recovers at 4 seconds.	It rises to 2400A and returns to permissible value around 3.5 seconds.	It increased to 1600A and regained its nominal value at 3 seconds.
Torque	Its control was lost until 4.1 seconds.	The machine control starts at 3.44 seconds.	The torque control was achieved at 3 seconds.
DC bus voltage	It overshoots to 1121V and follows its reference value around 4.2 seconds.	It expands to 1110V and stabilises at 3.7 seconds.	It increases to 1090V and chases its reference value at 3.3 seconds.

Thus, considering the above-stated comparative analysis, the proposed enhancing scheme performs more in terms of protecting the WTGS from abnormal situations and riding through the fault during severe voltage dips than the traditional and FLC crowbars.

CONCLUSIONS AND RECOMMENDATIONS

Conclusions

Doubly fed induction generators (DFIG) type wind powers are commonly utilised these days thanks to their requirement of low power electronic converter costs, independent regulation of reactive as well as active powers, and flexible wind speed operations. Despite these benefits, they are remarkably vulnerable to power network faults such as voltage sags as their stator terminals are directly attached to the power network/grid and their use of limited PEC ratings. A severe voltage drop at the grid terminal initiates to inrush both the generator stator as well as rotor currents, DC bus over voltages, and torque oscillations. In this situation, transmission system operators (TSO) require wind turbine generators to retain linked to the national grid. However, to obey the grid code requirements, these generators demand appropriate protection or enhancing schemes. So, in this thesis, a fuzzy logic controlled (FLC) hybrid crowbar and SDBR is employed. This enhancing technique is also compared with the conventional and fuzzy logic-controlled (FLC) crowbars to examine its effectiveness in enhancing the DFIG's performance under transient periods. When a balanced voltage dip takes place at the grid terminal, the stator voltage drops extensively, which forces it to enable the conventional crowbar for 100 milliseconds. At this moment, the converter control is inhibited and all current flows through the crowbar itself. Even though applying the conventional crowbar tried to improve the machine's low voltage ride-through (LVRT) capacity, the voltage recovery and the torque lost span were long. The FLC crowbar improved the timing of crowbar activation relative to the traditional one. The stator voltage recovery, torque control, and rotor current flow were fastened by 0.48, 0.56, and 0.5 seconds respectively. Moreover, with a hybrid fuzzy logic-controlled (FLC) crowbar and SDBR, the magnitudes of fault stator and rotor currents during crowbar activation were comparably lower than the previous ones. The timing of torque control, stator voltage return, and rotor current flow stability were also improved by 0.44, 0.28, and 0.5 seconds compared to FLC crowbar one respectively. Thus, the performance of DFIG is better improved by adopting the hybrid FLC crowbar and SDBR than the FLC crowbar and the conventional crowbar ones.

Recommendations

In this study, the effects of symmetrical voltage sags on the performance of DFIG-based WTGS while employing fuzzy logic controlled (FLC) crowbar and FLC hybrid crowbar with SDBR LVRT enhancing techniques were analysed.

So, this study recommends for Adama II wind power plant as well as other DFIG wind turbine owners to test this analysed hybrid FLC crowbar and series dynamic braking resistor LVRT enhancing scheme practically with a test rig device and implement it.

REFERENCES

Abad, G., López, J., Rodríguez, M., Marroyo, L., & Iwanski, G. (2011a). Direct Control of the Doubly Fed Induction Machine. In Doubly Fed Induction Machine: Modeling and Control for Wind Energy Generation Applications (pp. 363–477). Doubly Fed Induction Machine: Modeling and Control for Wind Energy Generation Applications. IEEE. https://doi.org/10.1002/9781118104965.ch8

Abad, G., López, J., Rodríguez, M., Marroyo, L., & Iwanski, G. (2011b). Steady State of the Doubly Fed Induction Machine. In Doubly Fed Induction Machine: Modeling and Control for Wind Energy Generation Applications (pp. 155–208). Doubly Fed Induction Machine: Modeling and Control for Wind Energy Generation Applications. IEEE. https://doi.org/10.1002/9781118104965.ch3

ABB. (2017). Wind turbine converters system description and start-up guide. https://library.e.abb.com/public/0b12d81db3b14f1ca103151ad2fa3e31/EN_ACS800-67_System_descr_B_A4.pdf

Abdelhamid, S., & Messaoud, H. (2021). DTC of DFIG included in a Wind Turbine Connected to the Grid. 2020 6th International Symposium on New and Renewable Energy (SIENR), 1–4. https://doi.org/10.1109/SIENR50924.2021.9631892

Abu-Rub, H., Malinowski, M., & Al-Haddad, K. (2014). Properties and Control of a Doubly Fed Induction Machine. In Power Electronics for Renewable Energy Systems, Transportation and Industrial Applications (pp. 270–318). Power Electronics for Renewable Energy Systems, Transportation and Industrial Applications. IEEE. https://doi.org/10.1002/9781118755525.ch10

Alam, M. S., Hossain, M. I., Hossain, M. A., Haque Choudhory, M. S., & Uddin, M. A. (2018). Protection of Inverter-based Distributed Generation with Series Dynamic Braking Resistor: A Variable Duty Control Approach. 2018 10th International Conference on Electrical and Computer Engineering (ICECE), 253–256. https://doi.org/10.1109/ICECE.2018.8636781

Al-Majed, S. I., & Fujigaki, T. (2010). Wind power generation: An overview. 2010 Modern Electric Power Systems, 1–6. https://ieeexplore.ieee.org/abstract/document/6007177/figures#figures

Amirul Bin Mohd Adnan, W. M., Bt Abdul Aziz, A., & Raya, L. B. (2022). Feasibility Study of Wind Power Generation System Using Small Scale Wind Turbines. 2022 IEEE 10th Conference on Systems, Process & Control (ICSPC), 166–169. https://doi.org/10.1109/ICSPC55597.2022.10001785

Davoudi, M., Sadeh, J., & Davoudi, M. (2019). Analysis of DFIG During Unsymmetrical Grid Fault by Using Crowbar Circuit. 2019 Iranian Conference on Renewable Energy & Distributed Generation (ICREDG), 1–6. https://doi.org/10.1109/ICREDG47187.2019.194198

Din, Z., Zhang, J., Xu, Z., Zhang, Y., & Zhao, J. (2021). Low voltage and high voltage ride-through technologies for doubly fed induction generator system: Comprehensive review and future trends. IET Renewable Power Generation, 15(3), 614–630. https://doi.org/10.1049/rpg2.12047

Djeriri, Y., Meroufel, A., & Massoum, A. (2014). Artificial neural network based direct torque control of doubly fed induction generator. Journal of Electrical Engineering, 14, 71–79.

Djidel, B., Mokrani, L., Machmoum, M., & Kouzou, A. (2022). Investigation of LVRT Capability of a DFIG Based WECS Under Different Grid Codes. 2022 19th International Multi-Conference on Systems, Signals & Devices (SSD), 86–91. https://doi.org/10.1109/SSD54932.2022.9955732

El Archi, C. Z., Nasser, T., & Essadki, A. (2019). Behavior of DFIG Based Wind System during Severe Voltage Dips. 2019 7th International Renewable and Sustainable Energy Conference (IRSEC), 1–6. https://doi.org/10.1109/IRSEC48032.2019.9078293

El-Jalyly, A., Derri, M., Haidi, T., & Janyene, A. (2019). Modeling and Control of a DFIG for wind Turbine Conversion System using Back-to-back PWM Converters. 2019 7th International Renewable and Sustainable Energy Conference (IRSEC), 1–6. https://doi.org/10.1109/IRSEC48032.2019.9078332

Endale, S. M., & Tuka, M. B. (2021). Fault Ride through Capability Analysis of Wind Turbine with Doubly Fed Induction Generator (2021070476). Preprints. https://doi.org/10.20944/preprints202107.0476.v1

Fdaili, M., Nasser, T., Essadki, A., Nadour, M., & Kharchouf, I. (2020). Control Strategies for DFIG-based Wind Turbine Systems Contributing to LVRT improvement and Grid Primary Frequency Adjustment. 2020 International Conference on Electrical and Information Technologies (ICEIT), 1–6. https://doi.org/10.1109/ICEIT48248.2020.9113195

Ganthia, B. P., Barik, S. K., & Nayak, B. (2020). Shunt Connected FACTS Devices for LVRT Capability Enhancement in WECS. Engineering, Technology & Applied Science Research, 10(3), Article 3. https://doi.org/10.48084/etasr.3560

Hazari, M. R., Mannan, M. A., Muyeen, S. M., Umemura, A., Takahashi, R., & Tamura, J. (2018). Stability Augmentation of a Grid-Connected Wind Farm by Fuzzy-Logic-Controlled DFIG-Based Wind Turbines. Applied Sciences, 8(1), Article 1. https://doi.org/10.3390/app8010020

Hiremath, R., & Moger, T. (2020). Comprehensive review on low voltage ride through capability of wind turbine generators. International Transactions on Electrical Energy Systems, 30(10), e12524. https://doi.org/10.1002/2050-7038.12524

Jayanthi, P., & Devaraj, D. (2019). Performance Study of DFIG Based Grid Connected WECS using Crowbar and Without Crowbar. 2019 IEEE International Conference on Intelligent Techniques in Control, Optimization and Signal Processing (INCOS), 1–3. https://doi.org/10.1109/INCOS45849.2019.8951426

Jayasawal, K., & Thapa, K. (2021). An Enhanced Low Voltage Ride-Through Control Scheme of a DIFG based WTG Using Crowbar and Braking Chopper. Journal of the Institute of Engineering, 16(1), 61–67. https://doi.org/10.3126/jie.v16i1.36537

Karkri, Y. E., Markhi, H. E., Lamhamdi, T., & Moussaoui, H. E. (2018). A comparison between Series Dynamic Resistors and CROWBAR circuit protection for LVRT capability of Doubly-Fed Induction Generator. IOP Conference Series: Earth and Environmental Science, 161(1), 012012. https://doi.org/10.1088/1755-1315/161/1/012012

Khan, F. H., Pal, T., Kundu, B., & Roy, R. (2021). Wind Energy: A Practical Power Analysis Approach. 2021 Innovations in Energy Management and Renewable Resources (52042), 1–6. https://doi.org/10.1109/IEMRE52042.2021.9386754

Kim, Y.-J., & Kim, H. (2016). Optimal inductance ratio of LCL filter for grid connected inverters considering with low order harmonics. IECON 2016 - 42nd Annual Conference of the IEEE Industrial Electronics Society, 2355–2360. https://doi.org/10.1109/IECON.2016.7793295

Milicua, A., & Abad, G. (2016). Control of grid-connected converters. In Power Electronics and Electric Drives for Traction Applications (pp. 148–220). John Wiley & Sons, Ltd. https://doi.org/10.1002/9781118954454.ch4

Mondragon Unibertsitatea (Director). (2017, May 3). DFIM Tutorial 5—Symmetrical Voltage Dips Analysis in DFIG based Wind Turbines [Video recording]. https://www.youtube.com/watch?v=9XzRuktDIqE

Okedu, K. E., Muyeen, S. M., Takahashi, R., & Tamura, J. (2011). Application of SDBR with DFIG to augment wind farm fault ride through. 2011 International Conference on Electrical Machines and Systems, 1–6. https://doi.org/10.1109/ICEMS.2011.6073472

Padhi, S. S., Krishna, P. B., Ray, P. K., & Mohanty, S. (2019). A Low Voltage Ride Enhancement Technique for Wind Energy System. 2019 National Power Electronics Conference (NPEC), 1–5. https://doi.org/10.1109/NPEC47332.2019.9034884

Pannell, G., Atkinson, D. J., & Zahawi, B. (2010). Minimum-Threshold Crowbar for a Fault-Ride-Through Grid-Code-Compliant DFIG Wind Turbine. IEEE Transactions on Energy Conversion, 25(3), 750–759. IEEE Transactions on Energy Conversion. https://doi.org/10.1109/TEC.2010.2046492

Park, K.-B., & Burkart, R. M. (2018). Filter Hardware Optimization of Grid-Tied Converters: LCL vs. LLCL Filter. 2018 7th International Conference on Renewable Energy Research and Applications (ICRERA), 209–214. https://doi.org/10.1109/ICRERA.2018.8566781

Qiuwei, W., & Yuanzhang, S. (Eds.). (2018). Grid Code Requirements for Wind Power Integration. In Modeling and Modern Control of Wind Power (pp. 11–36). Modeling and Modern Control of Wind Power. IEEE. https://doi.org/10.1002/9781119236382.ch2

Rauth, S. S., Kastha, D., & Bajpai, P. (2020). Comparative Analysis of External Configuration based DFIG-LVRT Enhancement Schemes. 2020 21st National Power Systems Conference (NPSC), 1–6. https://doi.org/10.1109/NPSC49263.2020.9331951

Rini Ann Jerin, A., Kaliannan, P., Subramaniam, U., & Shawky El Moursi, M. (2018). Review on FRT solutions for improving transient stability in DFIG-WTs. IET Renewable Power Generation, 12(15), 1786–1799. https://doi.org/10.1049/iet-rpg.2018.5249

Sahri, Y., Tamalouzt, S., & Belaid, S. L. (2018). Direct Torque Control of DFIG Driven by Wind Turbine System Connected to the Grid. 2018 International Conference on Wind Energy and Applications in Algeria (ICWEAA), 1–6. https://doi.org/10.1109/ICWEAA.2018.8605083

Sarkar, M. N. I., Meegahapola, L. G., & Datta, M. (2018). Reactive Power Management in Renewable Rich Power Grids: A Review of Grid-Codes, Renewable Generators, Support Devices, Control Strategies and Optimization Algorithms. IEEE Access, 6, 41458–41489. IEEE Access. https://doi.org/10.1109/ACCESS.2018.2838563

Sarwar, M., Hussain, B., Hussain, A., & Abubakar, M. (2019). Improvement of Fault Ride Through Capability of DFIG-based Wind Turbine Systems Using Superconducting Fault Current Limiter. 2019 IEEE Innovative Smart Grid Technologies - Asia (ISGT Asia), 4019–4024. https://doi.org/10.1109/ISGT-Asia.2019.8881155

Sourkounis, C., & Tourou, P. (2013). Grid Code Requirements for Wind Power Integration in Europe. Conference Papers in Science, 2013(1), 437674. https://doi.org/10.1155/2013/437674

Thomas, T., & Prince, A. (2020). LVRT capability evaluation of DFIG based wind energy conversion system under type-A and type-C grid voltage sags. 2020 IEEE International Conference on Power Electronics, Smart Grid and Renewable Energy (PESGRE2020), 1–6. https://doi.org/10.1109/PESGRE45664.2020.9070540

Tuka, M. B. (2020). DC Link Voltage and Power Flow Control of Doubly Fed Induction Generator in Wind Power System. 2020 IEEE PES/IAS PowerAfrica, 1–5. https://doi.org/10.1109/PowerAfrica49420.2020.9219862

Vozikis, D., Alsokhiry, F., Alabdulwahab, A., & Adam, G. (2020). Comparison of Conventional and Improved Two-level Converter during ac Faults. 2020 9th International Conference on Renewable Energy Research and Application (ICRERA), 352–358. https://doi.org/10.1109/ICRERA49962.2020.9242810

Wang, J., Wang, C., Rao, Y., Li, C., Liu, Y., Fang, Z., Cui, W., & Teng, W. (2019). Active Power Control Strategy of Wind Power Outgoing Channel Considering Multiple Constraints and Target Limit. 2019 IEEE Innovative Smart Grid Technologies - Asia (ISGT Asia), 1671–1676. https://doi.org/10.1109/ISGT-Asia.2019.8881065

WANG, R., SONG, H., HAN, L., YAN, L., WANG, B., & ZHAO, P. (2018). Study on LVRT of DFIG Wind Power System Based on Crowbar Protection Circuit. 2018 IEEE Student Conference on Electric Machines and Systems, 1–6. https://doi.org/10.1109/SCEMS.2018.8624855

Wu, Q., & Sun, Y. (Eds.). (2018). Modeling and modern control of wind power. John Wiley & Sons.

Xu, Z., Blaabjerg, F., Chen, W., & Zhu, N. (Eds.). (2018). Advanced control of doubly fed induction generator for wind power systems. Wiley IEEE press.

Zgarni, I., & El Amraoui, L. (2022). Dynamic Modeling and Vector control of DFIG-based Wind Turbine. 2022 5th International Conference on Advanced Systems and Emergent Technologies (IC_ASET), 262–267. https://doi.org/10.1109/IC_ASET53395.2022.9765917

Zou, Z.-C., Liao, J.-C., Lei, Y., Mu, Z.-L., & Xiao, X.-Y. (2019). Postfault LVRT Performance Enhancement of DFIG Using a Stage-Controlled SSFCL-RSDR. IEEE Transactions on Applied Superconductivity, 29(2), 1–6. IEEE Transactions on Applied Superconductivity. https://doi.org/10.1109/TASC.2019.2892821

APPENDICES

Appendix A

Table A.1: Parameters of Adama II Wind Turbine Generator System

Parameters	Values
Power rating	1.5MW
Rated frequency	50Hz
Stator voltage rating	690V
Rated stator current	1110A
Rotor open circuit voltage	1650V
Pole pairs	2
Rated speed	1800rpm
Rated torque	8341N.m
Slip	0.21
Turns ratio, u	0.42
Stator winding resistance	3.07mΩ
Rotor winding resistance	3mΩ
Leakage stator inductance, Lls	0.096mH
Leakage rotor inductance, Llr	0.157mH
Magnetising inductance, Lm	2.5mH
Inertia, J	$67Kg.m^2$
Vane length	37.75m
Gearbox ratio	94.7
Cpmax	0.486
Lambda optimum	9
DC bus voltage	1070V
DC bus capacitance	162 µF
Filter inductance, L	0.95mH
Filter capacitance, C	80.4µF
Crowbar resistance	0.45Ω
Maximum crowbar enable rotor current	1525V
Maximum crowbar enable DC voltage	1170V

Appendix B

Machine Transformations

The mathematical modelling of differential equations that express the behaviour of three-phase machines such as voltage, current, and flux are complex as they vary continuously in relative motion. So, transformations are applied to determine time-varying variables by referring to a common frame of reference. Among these mathematical transformation methods, Clarke and Park transformations are commonly used (Endale & Tuka, 2021).

Clarke Transformation

In this transformation, the three-phase balanced (a,b,c) are converted into balanced stationary two-phase (α,β) vectors according to the space vector representation provided in Figure (B.1) below.

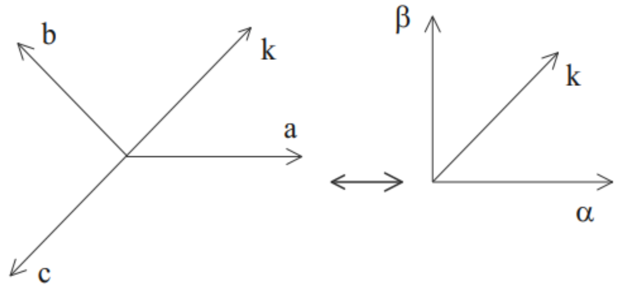

Figure B.1: Space Vector Representation in Stationary Frame (αβ axis) (Endale & Tuka, 2021)

Mathematically, this transformation in matrix form is represented by

$$\begin{pmatrix} k_\alpha \\ k_\beta \end{pmatrix} = \frac{1}{3}\begin{pmatrix} 2 & -1 & -1 \\ 0 & \sqrt{3} & -\sqrt{3} \end{pmatrix}\begin{pmatrix} k_a \\ k_b \\ k_c \end{pmatrix} \tag{B.1}$$

Its inverse transformation (from $\alpha\beta$ to abc) using equation (B.1) can be expressed by

$$\begin{pmatrix} k_a \\ k_b \\ k_c \end{pmatrix} = \frac{1}{2}\begin{pmatrix} 2 & 0 \\ -1 & \sqrt{3} \\ -1 & -\sqrt{3} \end{pmatrix}\cdot\begin{pmatrix} k_\alpha \\ k\beta \end{pmatrix} \tag{B.2}$$

Park Transformation

In this transformation. the two-phase balanced vectors from stationary reference (α, β) are converted into synchronous rotating (d, q) ones.

Analytically, it is given as

$$\begin{pmatrix} k_d \\ k_q \end{pmatrix} = \begin{pmatrix} \cos\theta_m & -\sin\theta_m \\ \sin\theta_m & \cos\theta_m \end{pmatrix} \cdot \begin{pmatrix} k_\alpha \\ k_b \end{pmatrix} \tag{B.3}$$

Where, θ_m stands for the angular shaft position in electrical and it is defined by

$$\theta_m = \int \omega_m dt \tag{B.4}$$

Similarly, its inverse transformation using expression (B.3) (from (dq) to ($\alpha\beta$)) is calculated by

$$\begin{pmatrix} k_\alpha \\ k_b \end{pmatrix} = \begin{pmatrix} \cos\theta_m & \sin\theta_m \\ -\sin\theta_m & \cos\theta_m \end{pmatrix} \cdot \begin{pmatrix} k_d \\ k_q \end{pmatrix} \tag{B.5}$$

Appendix C

Machine Side Converter Internal Simulink Models

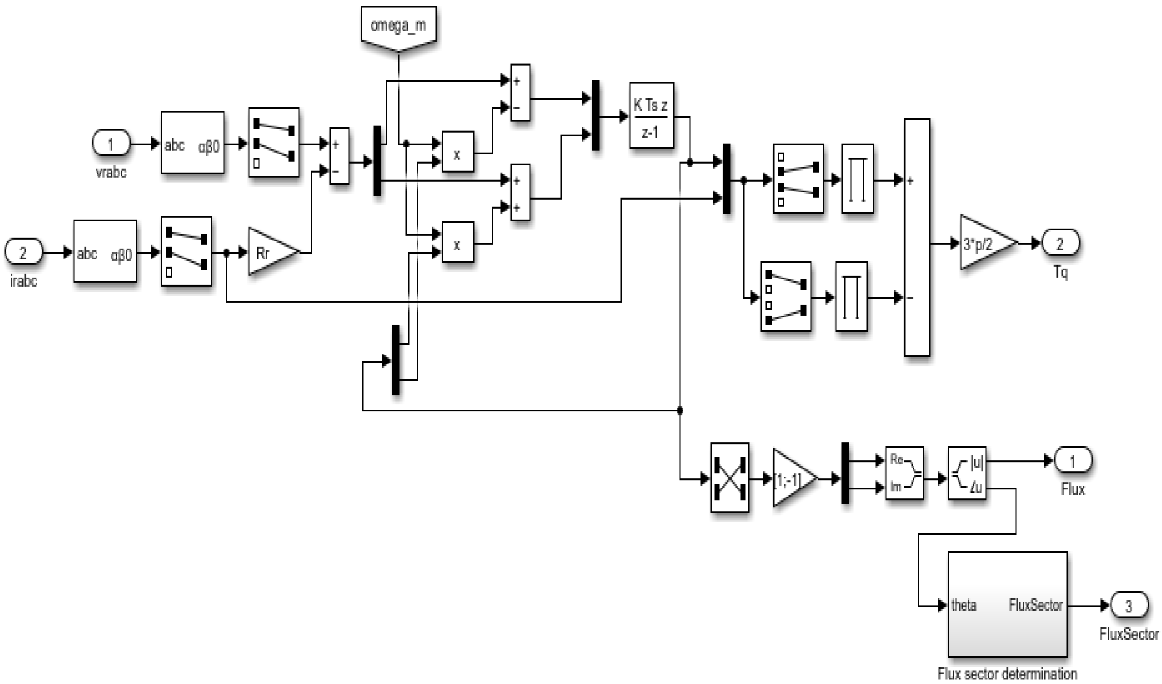

Figure C.1: Flux and Torque Estimator Model

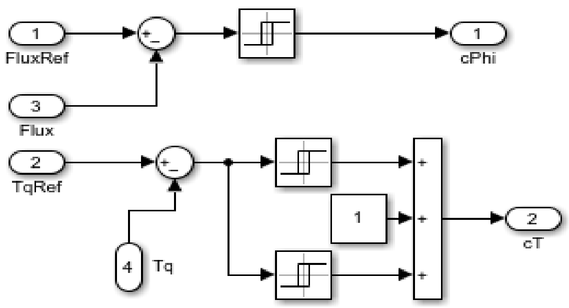

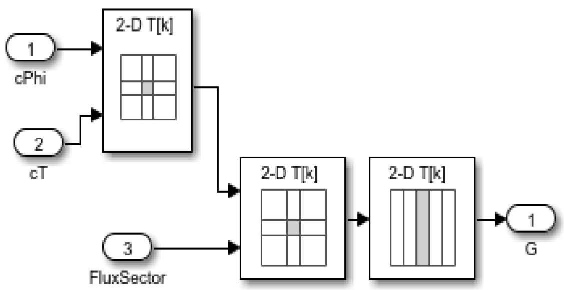

a) Flux and Torque Control b) Optimum Switching Table

Figure C.2: Vector Selection Model

Appendix D

MATLAB Code

```
% WTGS Parameters %
f=50;
Ps=1.5e6;
Ns=1500;
Vs=690;
Is=1110;
Tem=8341;
p=2;
Vr=1650;
u=0.42;
smax=0.21;
Rs=3.07e-3;
Rr=3e-3;
Lls=0.096e-3;
Llr=0.157e-3;
Lm=2.5e-3;
Ls=Lls+Lm;
Lr=Llr+Lm;
Vdc=1070;
Cb=162e-6;
Fs=Vs/(2*pi*f);
J=67;
D=1e-3;
Ts=2.5e-5;
% Wind Turbine Model %
ro=1.225;
g=94.7;
R=37.75;
beta=0;
ind2=1;
for lambda=0.1:0.01:13.4
    lambdai(ind2)=(1./((1./(lambda+0.08.*beta)-(0.035./(beta^3+1)))));
    Cp(ind2)=0.5176.*(116./lambdai(ind2)-0.4.*beta-5).*(exp(-
21./lambdai(ind2)))+0.0068.*lambda;
    Ct(ind2)=Cp(ind2)/lambda;
    ind2=ind2+1;
end
tab_lambda=[0.1:0.01:13.4];
figure
subplot(1,2,1)
plot(tab_lambda,Cp,'linewidth',1.5)
xlabel('lambda','fontsize',14)
ylabel('Cp','fontsize',14)
subplot(1,2,2)
plot(tab_lambda,Ct,'linewidth',1.5)
xlabel('lambda','fontsize',14)
```

```
ylabel('Ct','fontsize',14)
% MPPT %
Cpmax=0.486;
lambdaopt=9;
Kopt=((0.5*ro*pi*(R^5)*Cpmax)/(lambdaopt^3));
% LCL Filter %
L=0.95e-3;
C=80.4e-6;
% Crowbar Resistance Value %
Rc=0.45;
% Grid Side Converter and DC voltage PI Regulators %
wng=60*2*pi;
kpidg=(4*wng*L);
kpiqg=kpidg;
kiidg=2*(wnig^2)*L;
kiiqg=kiidg;
kpvdc=2*wng*Cb;
kivdc=(wng^2)*Cb;
kpg=1/(1.5*Vs);
kqg=-kpg;
% FLC Parameters %
Ir_max=1525;
Vdc_max=1170;
Vs_min=0.9*690;
```

Appendix E

Primary Data Validation

Generator and converter fault recorded between July 08, 2020 and July 07, 2024

Fault location		Quantity	Fault description
Generator	Rotor	51	Broken/cracked of their rotor terminals and/or burning of their slip rings
	Stator	4	Open or short circuit at their stator terminals
Back-to-back converter		93	IGBT and/or DC bus fuse failure
Crowbar		58	IGBT failure and/or total burnout

Adama II wind turbine generator system (WTGS) parameters

Parameters	Values
Rated power	1.5MW
Rated frequency	50Hz
Rated stator voltage	690V
Rated stator current	1110A
Rotor open circuit voltage	1650V
Pole pairs	2
Rated speed	1800rpm
Rated torque	8341N.m
Slip	0.21
Stator to rotor turns ratio, u	0.42
Stator winding resistance	3.07mΩ
Rotor winding resistance	3mΩ
Stator leakage inductance, Lls	0.096mH
Rotor leakage inductance, Llr	0.157mH
Magnetising inductance, Lm	2.5mH
Inertia	67Kg.m^2
Vane length	37.75m
Gearbox ratio	94.7
Cpmax	0.486
Lambda optimum	9
DC bus voltage	1070V
DC bus capacitance	162 μF
Filter inductance, L	0.95mH
Filter capacitance, C	80.4μF
Crowbar resistance	0.45Ω
Maximum crowbar enable rotor current	1525V
Maximum crowbar enable DC voltage	1170V

Ethiopian Federal Democratic Republic
Ethiopian Electric Power
Adama 2 Wind Power plant

Melese Silo
Adama 2 Wind Power Plant
Manager